

Non-uniform Superlattice Magnetic Tunnel Junctions

Sabarna Chakraborti* and Abhishek Sharma†

*Department of Electrical Engineering, Indian Institute of Technology Ropar
Nangal Rd, Hussainpur, Rupnagar, Punjab 140001*

(Dated: December 15, 2022)

The confluence of high packing density, low power consumption, and long-lasting memory retention have eventuated trilayer magnetic tunnel junctions (MTJs) for potential applications in the magnetic field sensors, non-volatile memories, and spin torque nano-oscillators. A modest tunnel magneto-resistance (TMR $\approx 100 - 300\%$) and a significant spin transfer torque switching bias of the traditional MTJs bottle-necked by the physics of single barrier tunneling, restrain the design landscape for futuristic high performance spintronics devices. We propose a new class of non-uniform superlattice magnetic tunnel junctions (Nu-SLTJs) with the Linear, Gaussian, Lorentzian, and Pöschl-teller width and height based profiles manifesting a sizable enhancement in the TMR ($\approx 10^4 - 10^6\%$) with a significant suppression in the switching bias (≈ 9 folds) owing to the physics of broad-band spin filtering. By exploring the negative differential resistance region in the current-voltage characteristics of the various Nu-SLTJs, we predict the Nu-SLTJs offer fastest spin transfer torque switching in the order of a few hundred picoseconds. We self-consistently employ the atomistic non-equilibrium Green's function formalism coupled with the Landau-Lifshitz-Gilbert-Slonczewski equation to evaluate the device performance of the various Nu-SLTJs. We also present the design of minimal three-barrier Nu-SLTJs having significant TMR ($\approx 10^4\%$) and large spin current for the ease of device fabrication. We hope that the class of Nu-SLTJs proposed in this work may lay the bedrock to embark on the exhilarating voyage of exploring various non-uniform superlattices for the next generation of spintronic devices.

I. INTRODUCTION

The research in the ambit of magnetic devices has witnessed an augmented proliferation with the development of magnetic tunnel junctions (MTJs) owing to their versatile applications in nanoscale spintronics. Ever since the pioneering discovery of tunnel magnetoresistance (TMR)[1] and spin transfer torque (STT)[2, 3], MTJs are being explored as the building blocks for energy-efficient integrated circuits of the beyond Moore era. Along with the STT-magnetoresistive random access memory (MRAM) and the spin torque nano oscillators (STNO), the utility of MTJs have been extended across the diverse disciplines of current imaging[4], magnetoencephalography[5], weapon detection[6], wireless communication[7], magnetic recording[8] and biomedical imaging[9]. Besides, the research of materializing the STT-MRAMs and the spin torque nano oscillators (STNOs) have predominantly anchored the novel literature of spintronic devices for their potential applications in the immediate future[10–17]. A confluence of high-speed operation, non-volatility, durability, and high density along with CMOS compatibility have eventuated the STT-MRAM as a viable candidate for state-of-the-art storage devices[18–21]. Apart from that, the broad tuning range[22], nanoscopic footprints[23], and effortless integration with cutting-edge CMOS technology have conferred the STNO a pivotal role in various frequency modulation schemes, wire-

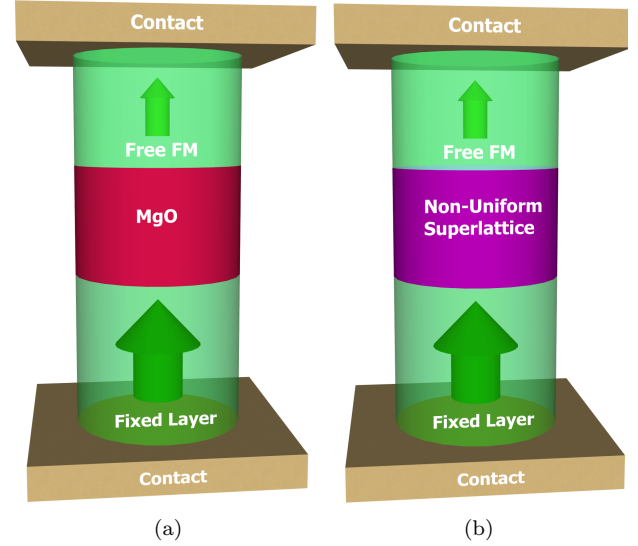


FIG. 1. Device schematics of a (a) trilayer MTJ with MgO as an insulator and (b) a non-uniform superlattice magnetic tunnel junction (Nu-SLTJ) featuring a non-uniform superlattice instead of the oxide layer.

less radio-frequency communication, and futuristic read heads[8, 24, 25].

A typical MTJ comprises a free and fixed ferromagnet (FM) separated by an insulating material (MgO)[26] as depicted in Fig. 1(a). An MTJ offers different resistances in the parallel (R_{PC}) and anti-parallel (R_{APC}) configurations of the magnetization of the fixed and free FMs due to spin-dependent tunneling of the electrons, which

* sabarna.20eez0025@iitrpr.ac.in

† abhishek@iitrpr.ac.in

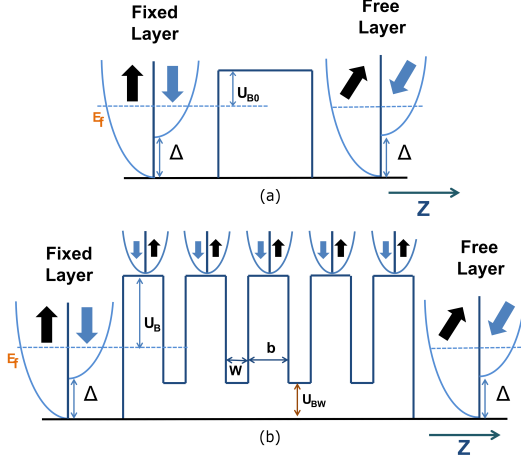


FIG. 2. (a) Band diagram of a conventional tri-layer MTJ and (b) a regular superlattice-based MTJ.

is quantified by the $TMR(\%) = (R_{PC} - R_{APC}) / (R_{APC}) \times 100\%$. The magnetization of the free FM can be switched using the STT exerted by the spin-polarized electrons coming from the fixed FM[2, 3, 27]. Perpendicular magnetic anisotropy (PMA) facilitates the magnetization of the fixed and free layers of the MTJ to align perpendicularly to the film plane. A typical PMA-MTJ (p-MTJ) yields fast switching in the order of a few nanoseconds along with lower power consumption and superior thermal stability compared to in-plane MTJs[28]. However, a faster switching demands a high current density that undermines the aspirations of energy-efficient writing[19, 29]. One may address this problem while applying the spin-orbit torque(SOT) to the free FM, where the switching current does not tunnel through the oxide layer of the MTJ, resulting in a significant reduction in power consumption[27]. But, SOT-switching is not deterministic in the p-MTJs, and one may need to apply some external magnetic field for deterministic switching[30]. At the same time, the separate reading and writing path in the SOT-driven MTJs increases the complexity of the fabrication process. Further, neither type of the devices (STT and SOT driven p-MTJs) yield an ultra-high sensitivity due to their inadequate $TMR(\%)$ in comparison to the proposed devices.

Technologically relevant applications based on the MTJ devices require a high $TMR(\%)$ and a low switching bias[31–33]. There have been consistent efforts to propose regular superlattice-based MTJs (SLTJs) to provide an ultra-high $TMR(\approx 10^5\%)$ and reduction in switching bias[34, 35] owing to the physics of spin selective resonant filtering. Along with these proposals, there have been consistent experimental efforts to realize superlattice-based MTJs(SLTJs) after the successful fabrications of various multiple-quantum well-based magnetic tunnel junctions[36–38]. Relying on this patronage, we propose a compendium of various nonuniform-SLTJs(Nu-SLTJs) for spintronic applications with the Gaussian,

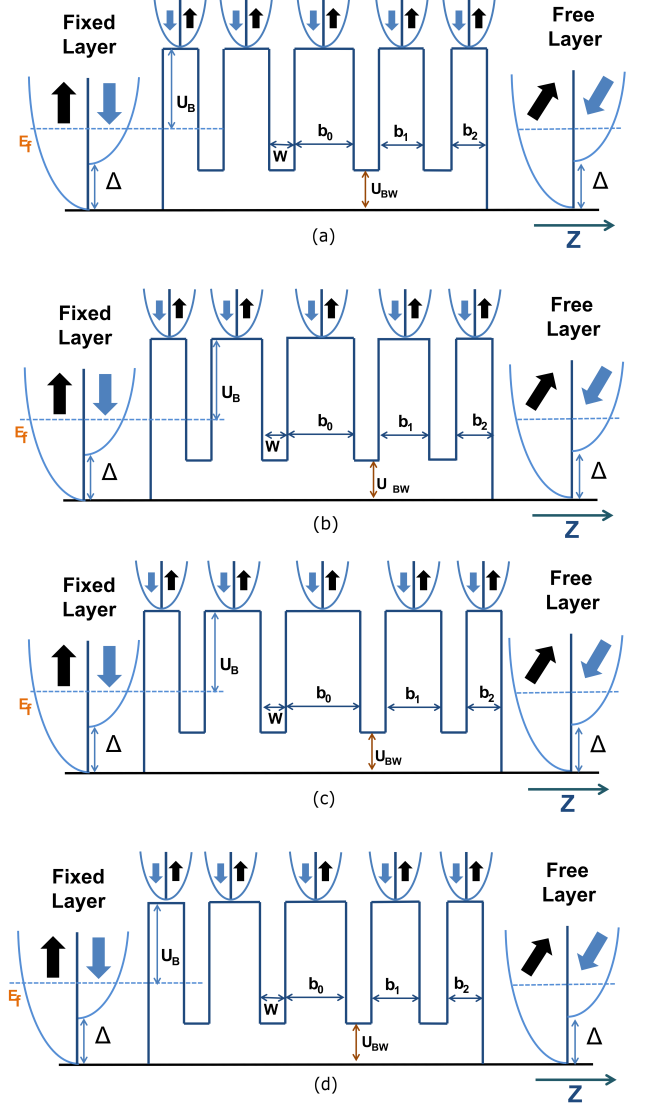


FIG. 3. Band diagram of the Nu-SLTJs with (a) Linear width (LW-SLTJ), (b) Gaussian width (GW-SLTJ), (c) Lorentzian width (LRW-SLTJ) and (d) Pöschl-Teller width (PW-SLTJ) profiles.

Linear, Lorentzian, and Pöschl-teller width(Fig. 3) and height(Fig. 4) profiles[39–41]. The physics of spin selective broad-band filtering (see Appendix A) in these proposed Nu-SLTJs culminates furtherance in the $TMR(\%)$ and a significant reduction in the switching bias of the proposed devices along with minimal layered Nu-SLTJs design.

In order to benchmark the switching biases of the various proposed devices (PDs) against the regular MTJ, we define a performance index as the suppression in the switching bias(SSB) given by

$$SSB = \frac{|SB_{MTJ}^{PC \rightarrow APC}| + |SB_{MTJ}^{APC \rightarrow PC}|}{|SB_{PD}^{PC \rightarrow APC}| + |SB_{PD}^{APC \rightarrow PC}|} \quad (1)$$

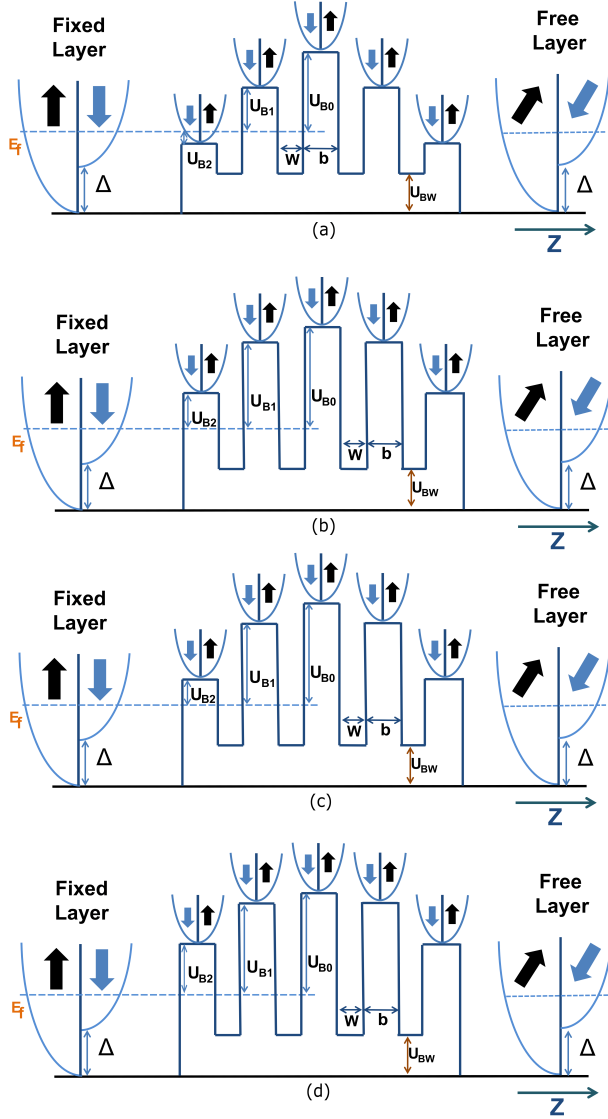


FIG. 4. Band diagram of the Nu-SLTJs with (a) Linear height (LH-SLTJ), (b) Gaussian height (GH-SLTJ), (c) Lorentzian height (LRH-SLTJ) and (d) Pöschl-Teller height (PH-SLTJ) profile.

where PC(APC) denotes the parallel(anti-parallel) configuration, $SB_{MTJ(PD)}^{APC \rightarrow PC}$ and $SB_{MTJ(PD)}^{PC \rightarrow APC}$ represents the switching biases applied to the trilayer MTJ(PD) for the APC to PC and the PC to APC switching, and SB represents the switching bias as discussed in Appendix A.

We chronicle this article by first describing the tight-binding device Hamiltonian and the self-consistent coupling of the Landau-Lifshitz-Gilbert-Slonczewski equation with the Non-equilibrium Green's Function formalism in section II, thereby providing a theoretical foundation behind our computational framework. Subsequently, we lay down the detailed design of various width(W) and height(H)-based Nu-SLTJs(W-SLTJs and H-SLTJs) along with the simulation re-

sults of each device in the section III. It incorporates the spin and charge current characteristics along with the switching dynamics of the various Nu-SLTJs comprised of Linear width(III B), Gaussian width(III C), Lorentzian width(III D), Pöschl-Teller width(III E), Linear height(III F), Gaussian height(III G), Lorentzian height(III H) and Pöschl-Teller height(III I) profiles including the trilayer MTJ(III A). We also demonstrate the relevance of the Nu-SLTJs in order to address the shortcomings of a regular SLTJ. Thereafter, we analyse the performances of the aforementioned devices at higher voltages in section IV while envisioning their possible applications in the STNOs. Thenceforth in section.V we compare various performance indices of the Nu-SLTJs in Tab.(I), followed by the conclusion in section VI, thereby abridging a synopsis of the study.

II. MATHEMATICAL MODELLING AND SIMULATION DETAILS

We begin with the description of the device schematics of the tri-layer MTJ and the Nu-SLTJ depicted in Figs. 1(a) and 1(b). The Nu-SLTJ is realized by sandwiching a non-uniform heterostructure comprised of insulator(I)-normal metal(NM)-I-NM-I-NM-I layers between the fixed and free FMs as shown in Figs.3&4. We have used MgO as an insulator to implement the W-SLTJs, whereas H-SLTJs have been realized by utilizing a stoichiometrically substituted $Mg_xZn_{1-x}O$ [42] as barrier region. The quantum(q)-well regions of the non-uniform superlattice may consist of an NM (Ru,Pt,Cu,Ti,W etc.) such that the dimension of the q-wells remain significantly smaller than spin coherent length[34, 35, 43, 44].

To analyse the quantum transport through mesoscopic devices such as an MTJ or an Nu-SLTJ, we first describe the relationship of the Hamiltonian matrix $[H]$ with the energy-resolved spin-dependent retarded Green's function matrix $[G(E)]$, given by[45]

$$[G(E)] = [EI - \Sigma - H]^{-1} \quad (2)$$

$$[\Sigma] = [\Sigma_F] + [\Sigma_f] \quad (3)$$

where the Hamiltonian matrix $[H]=[H_0]+[U_0]$ comprises the nearest neighbour tight-binding Hamiltonian $[H_0]$ and the applied potential matrix $[U_0]$, while I represents an identity matrix with dimensions of the device Hamiltonian $[H]$. In equation.3, we formulate the coupling of the Hamiltonian matrix corresponding to the device region $[H]$ with the self-energy matrices of the fixed and the free FMs described via Σ_F and Σ_f , respectively. We describe the ferromagnetic behavior of the contacts by the Stoner model [46], with conduction band exchange splitting (Δ), Fermi energy (E_f), and effective mass (m_{fm}). Based on the above-mentioned formulation, we compute the Hamiltonian matrix $[H]$, the self-energy matrix (Σ), and the energy-resolved spin-dependent retarded Green's function matrix $[G(E)]$ for the tight binding framework[43]. In order to take care

of the current conduction at various modes, we include the respective transverse mode energies(E_t) to the diagonal elements of the device Hamiltonian given by $E_t = \hbar^2 k_x^2 / 2m^* + \hbar^2 k_y^2 / 2m^*$, where k_x and k_y represents wave vectors along the x and y axis, while the electron transport takes place along the z direction. [43].

In the next step, we describe the density of electrons

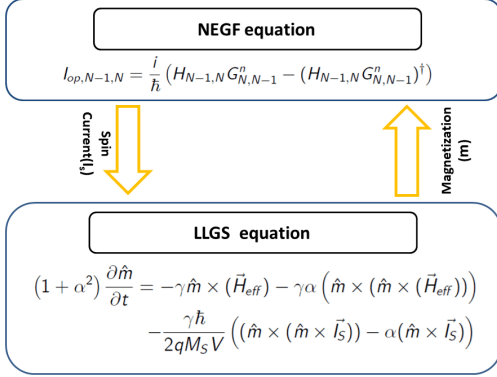


FIG. 5. The self consistent coupling of the non-equilibrium Green's function with the Landau-Lifshitz-Gilbert-Slonczewski equation.

in the channel region by the diagonal elements of the energy resolved electron correlation matrix $[G^n(E)]$, given by

$$[G^n] = \int [G(E)][\Sigma^{in}(E)][G(E)]^\dagger dE \quad (4)$$

$$[\Sigma^{in}(E)] = [\Gamma_F(E)]f_F(E) + [\Gamma_f(E)]f_f(E) \quad (5)$$

where the quantities $[\Gamma_F(E)] = i([\Sigma_F(E)] - [\Sigma_F(E)]^\dagger)$ and $[\Gamma_f(E)] = i([\Sigma_f(E)] - [\Sigma_f(E)]^\dagger)$ denotes the spin-dependent broadening matrices [47] of the fixed and free FM contacts, respectively. To construct the applied potential matrix $[U_0]$, we assume a linear drop across the oxide region and no drop across the metal layers. The Fermi-Dirac distribution functions related to the free(f) and fixed(F) FMs are denoted as $f_f(E)$ and $f_F(E)$, respectively. We apply the boundary conditions by assuming $U_{FixedFM} = -qV/2$ and $U_{FreeFM} = qV/2$, where V is the applied voltage. The current between $N-1$ th and N th lattice points of the device is described by the current operator I_{op} [48], given by

$$I_{op,N-1,N} = \frac{i}{\hbar} (H_{N-1,N} G_{N,N-1}^m - (H_{N-1,N} G_{N,N-1}^m)^\dagger) \quad (6)$$

The charge current through the device I is defined as

$$I = q \int \text{Real} [\text{Trace}(\hat{I}_{op})] dE \quad (7)$$

and spin current I_S is given by

$$I_{S_i} = q \int \text{Real} [\text{Trace}(\sigma_i \cdot \hat{I}_{op})] dE \quad (8)$$

where σ_i denotes the Pauli spin-matrices along \hat{x} , \hat{y} , \hat{z} directions.

The magnetization dynamics of the free layer in the presence of an applied magnetic field and spin current is calculated using the self consistent coupling of the NEGF formalism with the Landau-Lifshitz-Gilbert-Slonczewski (LLGS) equation as described in Fig. 5. The LLGS equation[3] is given by

$$(1 + \alpha^2) \frac{\partial \hat{m}}{\partial t} = -\gamma \hat{m} \times \vec{H}_{eff} - \gamma \alpha (\hat{m} \times (\hat{m} \times \vec{H}_{eff})) - \frac{\gamma \hbar}{2qM_s V} ((\hat{m} \times (\hat{m} \times \vec{I}_s)) - \alpha (\hat{m} \times \vec{I}_s)) \quad (9)$$

where \hat{m} represents the direction of magnetization of the free layer, α represents the Gilbert damping parameter and γ is called the gyromagnetic ratio of the electron, M_s represents the saturation magnetization, V represents the volume of the FM contacts. The effective magnetic field is given by $\vec{H}_{eff} = \vec{H}_{applied} + \vec{H}_{k\perp} m_z \hat{z}$, with $\vec{H}_{applied}$ being the applied field which is taken as zero for our simulations, and $\vec{H}_{k\perp} \vec{m}_z$ represents the uniaxial magnetic anisotropy of the FMs with PMA.

The spin current is decomposed into three components such that

$$\vec{I}_S = I_{s,m} \hat{m} + I_{s,\parallel} \hat{M} + I_{s,\perp} \hat{M} \times \hat{m}$$

where \hat{M} and \hat{m} represents a unit vector along the direction of the fixed and free FM, respectively and apart from that the $I_{s,\parallel}$ and $I_{s,\perp}$ denotes the Slonczewski and field like term.

Further, the equation.9 can be divided in two factors such that

$$(1 + \alpha^2) \frac{\partial \hat{m}}{\partial t} = \text{Spinning factor} + \text{Damping factor} \quad (10)$$

where, the spinning factor(SF) describes the angular frequency of the magnetization around the easy axis and the damping factor(DF) represents the rate of change of the angle between the easy axis and the magnetization.

After plugging in the value of the \vec{I}_s in equation.9 the spinning factor(SF) can be re-casted as

$$SF = -\gamma \left(\hat{m} \times \vec{H}_{eff} + \frac{\hbar}{2qM_s V} (I_{s,\perp} - \alpha I_{s,\parallel}) \hat{m} \times \hat{M} \right) \quad (11)$$

Similarly, the expression of the damping factor(DF) can be simplified as

$$DF = -\gamma \alpha (\hat{m} \times \hat{m} \times \vec{H}_{eff}) + \frac{\gamma \hbar}{2qM_s V} (I_{s,\parallel} + \alpha I_{s,\perp}) \hat{m} \times \hat{m} \times \hat{M} \quad (12)$$

We can safely ignore the term $\alpha I_{s,\perp}$ in Eq. 12 as it is much smaller than $I_{s,\parallel}$. Hence, the critical current for switching is given as $I_{s,\parallel,c} = \frac{2qM_s V \alpha}{\hbar} H_{eff}$.

The value of the critical switching current for an in plane MTJ under the macro-spin assumption is given by $I_{s||,c} = \frac{2\alpha e}{\hbar} VM_s(H_K + H_d/2)$, where H_K and H_d denotes the in-plane anisotropy and the demagnetizing field, respectively[49]. It is worthwhile mentioning that the value of the H_d is mostly one order higher compared to the H_K which causes a significant hike in power consumption. One may reduce the impact of the H_d while utilizing FMs with PMA[50], where the direction of the magnetization aligns perpendicularly to the thin film plane[51]. The effective magnitude of the perpendicular anisotropy is given as $H_{K\perp} = 2\frac{\sigma}{tM_s} - H_d$, where t and σ denotes the thickness and the interface PMA factor of an FM thin film, respectively. The inter-facial PMA dominates the H_d when the width of the FM is made smaller beyond a critical thickness[52]. The value of the critical current is given by $I_{s||,c} = \frac{2qM_sV\alpha}{\hbar} H_{K\perp}$.

In this work, we have used CoFeB for the FM contacts with the Fermi energy $E_f = 2.25$ eV and conduction band exchange splitting $\Delta = 2.15$ eV[44] while assuming the effective masses of an electron in the MgO barriers, in the NM quantum wells and in the FM contacts as $m_{ox} = 0.18m_e$, $m_{nm} = 0.9m_e$ and $m_{fm} = 0.8m_e$, respectively [53], where m_e denotes the free-electron-mass. We have taken the barrier height between CoFeB and MgO as $U_B = 0.76$ eV above Fermi level [54] and considered the conduction band offset between the FM and the NM layer as $U_{BW} = 0.4$ eV. The NM q-wells have the same thickness of $W = 0.35$ nm to keep them within the fabrication limits [36, 55]. We have considered the minimum oxide width as 0.6 nm which is the least thickness of the MgO that can be deposited reliably [56]. We have taken the thickness of the free FM as 1.3 nm [52] and have considered the cross-sectional area of the FM contacts as $0.25\pi \times 30^2$ nm² so that the magnetization dynamics of the free FM can be described by a macro-spin model [57]. The value of the saturation magnetization is considered as $M_s = 1150$ emu/cc and the perpendicular uni-axial magnetic anisotropy is taken as $H_{k\perp} = 3.3$ kOe[58]. The thermal stability factor is given by $\Delta_{EB} = H_K M_s V / 2k_B T \approx 42$. The value of the damping parameter and gyromagnetic ratio are taken as $\alpha = 0.01$ and $\gamma = 17.6$ MHz/Oe, respectively.

After evaluating all the parameters in the equation of the critical current given by $I_{s||,c} = \frac{2qM_sV\alpha}{\hbar} H_{k\perp}$, we obtain an $I_{s||,c}$ of 0.0106 mA. When the $I_{s||}$ becomes equal to the $I_{s||,c}$, the damping force (DF) acting on the free layer becomes zero and the relative angle (θ) between the easy axis and magnetization of the free layer becomes constant. In order to perform the switching of the free FM, we need to supply a switching current, higher than the critical current, so that the spin current ($I_{s||}$) induced anti-damping force ($\frac{\hbar}{2qM_sV} I_{s||} \hat{m} \times \hat{m} \times \hat{M}$) dominates over the damping due to the uniaxial magnetic anisotropy ($-\gamma(\alpha(\hat{m} \times \hat{m} \times H_{eff}))$). Whilst the $I_{s||}$ is near the critical current, the effective damping force acting on the free layer becomes negligible. Hence the switching of the magnetization takes a longer time. To avoid this,

we apply a spin current ($I_{s||} = 0.0127$ mA), which is 20% higher than the critical current (see Appendix:A) thereby ensuring a comfortable switching.

III. DEVICE DETAILS AND SIMULATION RESULTS

In the wide design landscape of non-uniform superlattices, we first explore the TMR(%) and $I_{s||}$ of various Nu-SLTJs with respect to the number of barriers (oxide layers) as shown in the Fig. 6 (at $V=5$ mV). It can

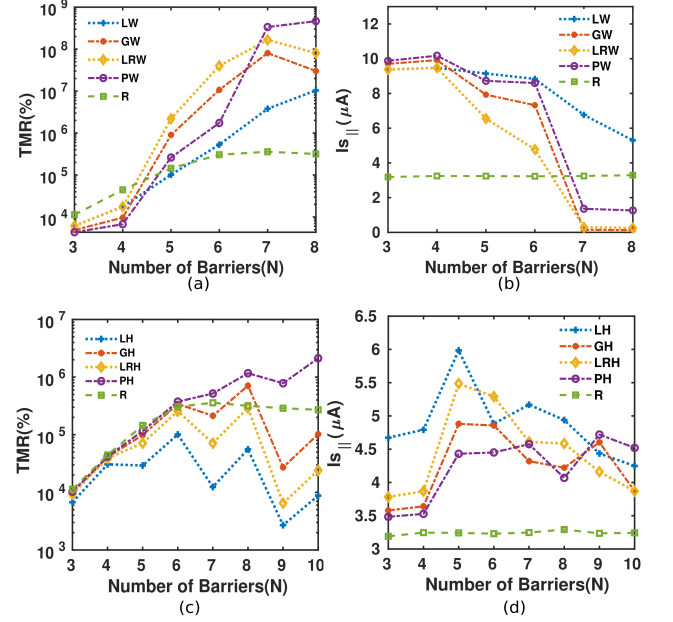


FIG. 6. (a) TMR(%) and (b) $I_{s||}$ of the W-SLTJs, (c) TMR(%) and (d) $I_{s||}$ of the H-SLTJs with respect to the number of barriers at $V=5$ mV. Here, LW represents Linear width, GW represents Gaussian width, LRW represents Lorentzian width, PW represents Pöschl-Teller width, LH represents Linear height, GH represents Gaussian height, LRH represents Lorentzian height, PH represents Pöschl-Teller height and R represents Regular superlattice.

be inferred from Fig. 6(a) & (b) that in W-SLTJs, the TMR(%) first increases with the number of barriers and then decreases whereas $I_{s||}$ decreases monotonically. As the number of barriers (N) goes from 4 to 5, we see a significant increase in the TMR(%) along with a respectable $I_{s||}$. At $N=6$, although a higher TMR(%) is achieved but $I_{s||}$ drops even further. In our design of width-based SLTJs, the thickness of the central barriers increases with N to keep the width of terminal barriers within fabrication limits [56]. The thickness of the central oxide in the GW-SLTJ reaches 2.1 nm at $N = 7$ because of the exponent factor $e^{-x^2/7}$ (see Eq. 13). It vanishes the spin selective transmission through the GW-SLTJ for $N > 6$, resulting in a decimated $I_{s||}$. A similar behaviour is noticed for both the PW and LRW-SLTJs making them

dysfunctional for $N > 6$ except for the LW-SLTJ.

We present the dependence of the TMR(%) and $I_{s||}$ of the H-SLTJs with respect to the number of barriers in Fig. 6. Figure. 6(c)&(d) illustrates that the $I_{s||}$ of the H-SLTJs peaks at $N=5$ along with a sizeable TMR(%).

Hence, in the subsequent subsections, we present detailed designs of the W and H-SLTJs with $n=5$ and draw a performance comparison with a regular SLTJ and a trilayer MTJ in Tab. I. Figure. 6 exemplifies that the regular SLTJ(R-SLTJ) offers an adequate TMR(%) in comparison to the Nu-SLTJs but fails to provide a respectable $I_{s||}$. Hence, Nu-SLTJs emerge as viable alternatives for meager power consumption and faster switching.

A. Characteristics of a Tri-layer MTJ

We first explore the electrical characteristics of a trilayer MTJ shown in Fig. 1(a), along with the STT-switching of the free FM. The device consists of an MgO

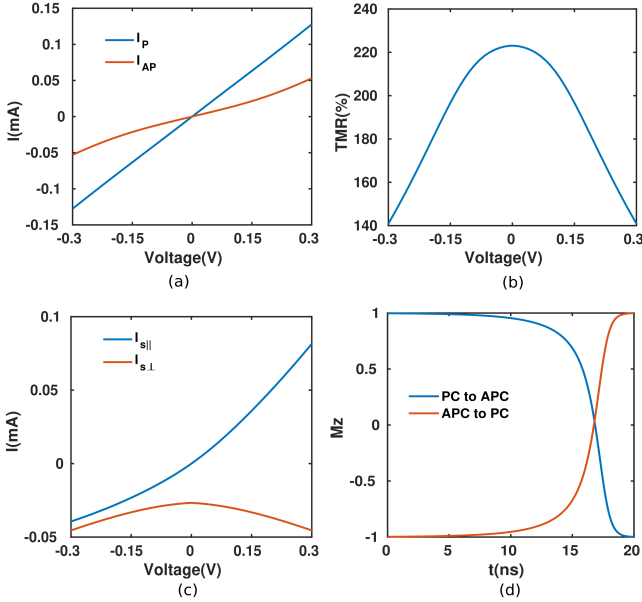


FIG. 7. (a) I-V characteristics of the MTJ in the PC(I_P) and APC(I_{AP}). (b) Variation of TMR(%), (c) $I_{s||}$ and $I_{s\perp}$ with the applied voltage. (d) STT based switching of the free layer from the PC to APC($V=-74$ mV) and the APC to PC($V=60$ mV).

barrier of 1 nm thickness sandwiched between fixed and free FMs. The band diagram of the device is shown in Fig. 2(a). We show the I-V characteristics of the device in the PC and the APC in Fig. 7(a). The maximum TMR(%) provided by the tri-layer MTJ is 240%(Fig. 7(b)). Figure. 7(d) illustrates the STT-switching of the free layer from the APC to PC and the PC to APC at switching-bias of 60 mV and -74 mV, respectively(see Appendix: A). The difference in magnitude of the $SB^{PC \rightarrow APC}$ and $SB^{APC \rightarrow PC}$ originates from the

asymmetrical $I_{s||} - V$ relationship of the device as shown in Fig. 7(c). The TMR and spin current of the trilayer MTJ can be reasoned out from spin selective transmission spectra of the PC (see Fig. 20(a)) and the APC (see Fig. 20(b)) enabled by physics of single barrier tunneling.

B. Device characteristics of Linear Width based Nu-SLTJ (LW-SLTJ)

To construct the linear width(LW) based Nu-SLTJ shown in Fig. 3(a), we consider the width of n -th(b_n) barrier as

$$b_n = b_0 - n \times 0.15$$

where $b_2 = 0.6$ nm and $n=0,1,2$. The $n = 0$ represents the central barrier, $n = 1$ represents the two neighbour barriers of the central barrier, and $n = 2$ represents the two terminal barriers. In Fig. 8(a) we present

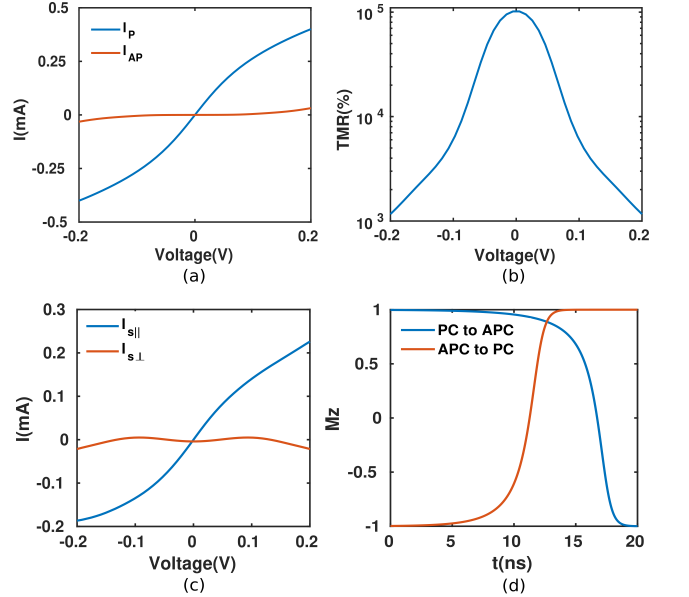


FIG. 8. (a) I-V characteristics of the LW-SLTJ in the PC(I_P) and APC(I_{AP}). (b) Variation of TMR(%), (c) $I_{s||}$ and $I_{s\perp}$ with the applied voltage. (d) STT based switching of the free layer from the PC to APC($V=-7.4$ mV) and the APC to PC($V=7.4$ mV).

the I-V characteristics of the LW-SLTJ in the PC and the APC. The maximum TMR(%) provided by the device is $\approx 10^5\%$. Figure 8(d) shows the STT-switching of the free layer from the PC to APC and the APC to PC with $SB^{PC \rightarrow APC}$ and $SB^{APC \rightarrow PC}$ of -7.4 mV and 7.4 mV, respectively. Unlike the trilayer MTJ, the $I_{s||} - V$ characteristics of the LW-SLTJ is nearly symmetrical around 0V(Fig. 8(c)). Hence the magnitude of switching biases remains the same in both the cases. The sizable ratio of the LW-SLTJ enabled transmissions in the

PC(Fig.17(a)) and APC(Fig.17(b)) provides to a monumental enhancement in the TMR(%) as shown in Fig. 8(b). Furthermore, the broad-band spin filtering exhibited by the LW-SLTJ device provides a sizable $I_{s||}$ which reduces the switching bias substantially, thereby yielding the largest SSB of 9.05(see Tab. I).

C. Device characteristics of Gaussian Width based Nu-SLTJ (GW-SLTJ)

We characterize the thickness of the n -th barrier(b_n) in the Gaussian width(GW) based Nu-SLTJ in such a way that

$$b_n = b_0 e^{-n^2/7} \quad (13)$$

where $b_2 = 0.6$ nm and $n=0,1,2$. The band diagram of the device is presented in Fig. 3(b). In Fig 9(a), we present the I-V characteristics of the GW-SLTJ in the PC and the APC. The maximum TMR(%) yielded by the device is \approx

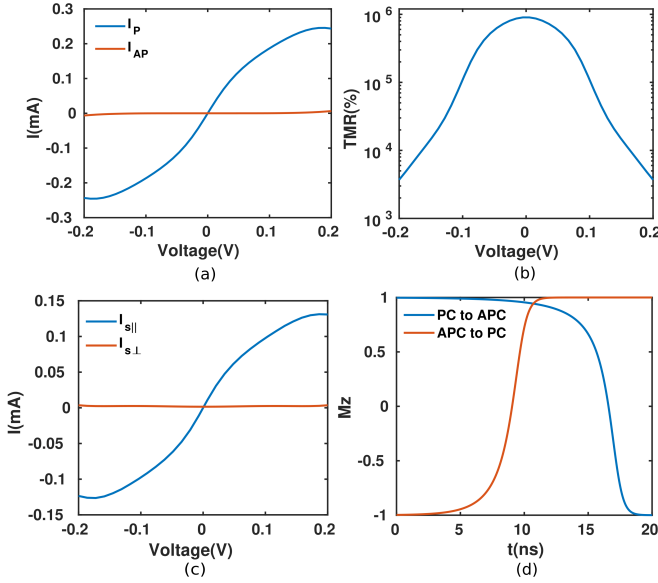


FIG. 9. (a) I-V characteristics of the GW-SLTJ in the PC(I_P) and APC(I_{AP}). (b) Variation of TMR(%), (c) $I_{s||}$ and $I_{s\perp}$ with the applied voltage. (d) STT based switching of the free layer from the PC to APC($V=-8.88$ mV) and the APC to PC($V=8.88$ mV).

$9.01 \times 10^5\%$ (Fig. 9(b)). Similar to the LW-SLTJ, the $I_{s||}$ -V characteristics of the GW-SLTJ is nearly symmetrical around 0V(Fig. 9(c)). Therefore the magnitudes of the $SB^{PC \rightarrow APC}$ and $SB^{APC \rightarrow PC}$ remain the same. In Fig. 9(d) we present the STT-switching of the free layer in the GW-SLTJ for $I_{s||}=0.0127$ mA. The applied voltages for the PC to APC and the APC to PC switching are -8.88 mV and 8.88 mV, respectively. Therefore, the SSB achieved in this case is 7.61, the 3rd largest among all the Nu-SLTJs(see Tab. I). Similar to the LW-SLTJ, the

significant enhancement in the TMR(%) and $I_{s||}$ that we accomplish via GW-SLTJ can be rationalized in light of the spin selective broad-band filtering offered by the GW-SLTJ as shown in Figs. 17(c)&(d).

D. Device characteristics of Lorentzian Width based Nu-SLTJ(LRW-SLTJ)

The Lorentzian-width(LRW) based Nu-SLTJ is engineered in such a way that the width of n -th barrier(b_n) is given by

$$b_n = b_0 \left(\frac{\Gamma^2}{\Gamma^2 + n^2} \right)$$

where $b_2 = 0.6$ nm and $\Gamma=2$. We present the band diagram of the device in Fig. 3(c). Figure. 10(a) shows

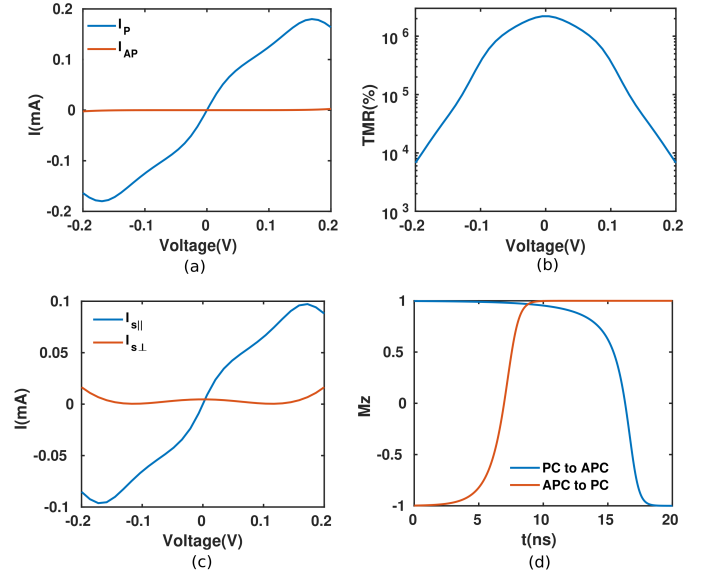


FIG. 10. (a) I-V characteristics of the LRW-SLTJ in the PC(I_P) and APC(I_{AP}). (b) Variation of TMR(%), (c) $I_{s||}$ and $I_{s\perp}$ with the applied voltage. (d) STT based switching of the free layer from the PC to APC($V=-11.7$ mV) and the APC to PC($V=11.7$ mV).

the I-V characteristics of the LRW-SLTJ in the PC and the APC. The maximum TMR(%) obtained for this device is $2.19 \times 10^6\%$ (Fig. 10(b)). We present the variation of the $I_{s||}$ and $I_{s\perp}$ with the applied voltage in Fig. 10(c). The switching dynamics of free FM in the SLTJ is presented in Fig.10(d) with the $SB^{APC \rightarrow PC}$ and $SB^{PC \rightarrow APC}$ of -11.7 mV and 11.7 mV, respectively. The LRW-SLTJ provides the 5th largest SSB with 5.73 (see Tab. I). The superiority of the performance indices in terms of the TMR(%) and the $I_{s||}$ that we realize through the LRW-SLTJ can be reasoned out on the basis of the heterostructure enabled broad-band spin filtering in the PC and APC as shown in Figs. 17(e)&(f).

E. Device characteristics of the Pöschl-Teller Width based Nu-SLTJ(PW-SLTJ)

The Pöschl-Teller width based Nu-SLTJ is constructed in such a way that the thickness of n -th barrier is given by

$$b_n = b_0 \frac{2}{e^{n/2} + e^{-n/2}}$$

where b_2 is 0.6 nm and $n = 0, 1, 2$. The band diagram of the device is shown in Fig. 3(d). In Fig. 11(a) we

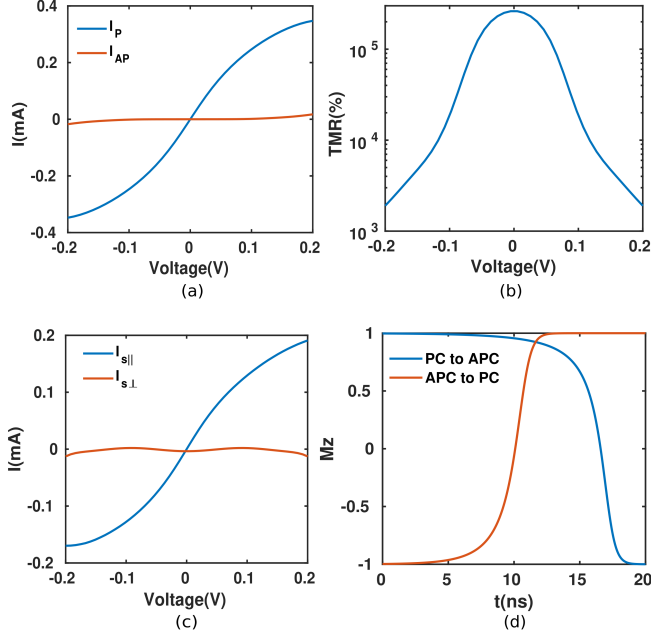


FIG. 11. (a) I-V characteristics of the PW-SLTJ in the PC(I_P) and APC(I_{AP}). (b) Variation of TMR(%), (c) $I_{s||}$ and $I_{s\perp}$ with the applied voltage. (d) STT based switching of the free layer from the PC to APC($V=-7.75$ mV) and the APC to PC($V=7.75$ mV).

present the I-V characteristics of the PW-SLTJ in the PC and the APC. The maximum TMR(%) offered by the device is nearly 2.61×10^5 (%). Fig. 11(d) depicts the STT-switching of the free layer from the PC to APC and the APC to PC with the $SB^{PC \rightarrow APC}$ and $SB^{APC \rightarrow PC}$ of -7.75 mV and 7.75 mV, respectively. Hence, the SSB obtained in this case is 8.7 (see Tab. I), the second largest after the LW-SLTJ. The broad-band spin filtering in the PW-SLTJ (see Fig. 17(g)&(h)) enables the device to accomplish a remarkable enhancement in the TMR(%) and the $I_{s||}$ as shown in Fig. 11(b) and 11(c).

F. Device characteristics of the Linear Height based Nu-SLTJ(LH-SLTJ)

Along with different width profiles, the Nu-SLTJs with different height profiles also substantiate their worth as

potential candidates for high-performance MTJs. Hence, in the subsequent subsections, we present the height-based analogues of the above-mentioned heterostructures geared towards broad-band spin filtering.

At first we devise the Linear height(LH) based Nu-

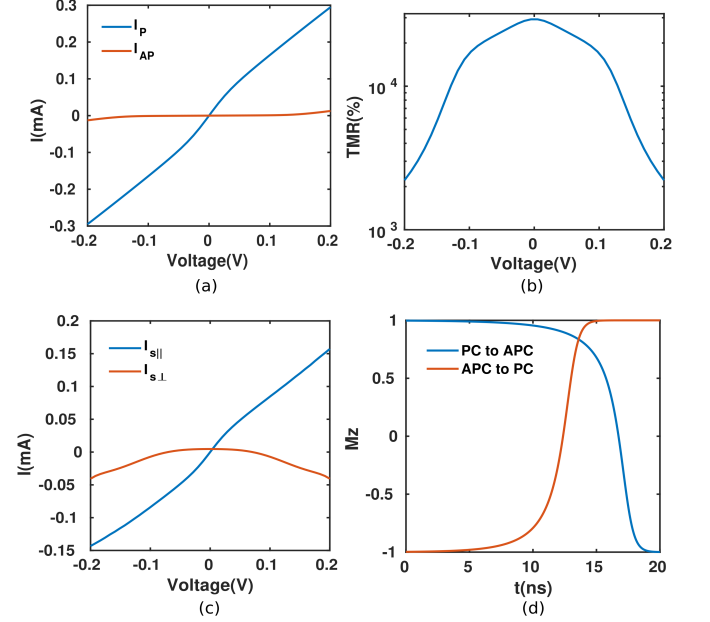


FIG. 12. (a) I-V characteristics of the LH-SLTJ in the PC(I_P) and APC(I_{AP}). (b) Variation of TMR(%), (c) $I_{s||}$ and $I_{s\perp}$ with the applied voltage. (d) STT based switching of the free layer from the PC to APC($V=-11.6$ mV) and the APC to PC($V=11.6$ mV).

SLTJ as shown in Fig. 4(a), where the scattering potential of the n -th barrier ($SP_n = E_f + U_{Bn}$) is given by

$$E_f + U_{Bn} = (E_f + U_{B0}) - 0.4n$$

with $SP_0 = E_f + U_{B0} = 3.01$ eV representing the central barrier, $SP_1 = E_f + U_{B1} = 2.61$ eV representing the two neighbour barriers of the central barrier, and $SP_2 = E_f + U_{B2} = 2.21$ eV representing the two terminal barriers. We have used MgO to implement the central barrier, and the rest of the barriers are realized by stoichiometrically substituted $Mg_xZn_{1-x}O$ where x is substituted in accordance to design the respective scattering potentials.

In Fig. 12(a), we present the I-V characteristics of the LHSLTJ in the PC and the APC. The maximum TMR(%) provided by the device is approximately $\approx 2.9 \times 10^4$ (%) (Fig. 12(b)). Figure. 12(d) depicts the switching dynamics of the free layer with the $SB^{PC \rightarrow APC}$ and $SB^{APC \rightarrow PC}$ of -11.6 mV and 11.6 mV, respectively. Therefore, the LH-SLTJ provides an SSB of 5.8, the 4th largest among all the NU-SLTJs (see Tab. I). Similar to the W-SLTJs, the ratio of transmissions in the PC (Fig. 19(a)) and APC (Fig. 19(b)) is the cornerstone of the towering TMR(%) we accomplish via LH-SLTJ. In addition to this, the large $I_{s||}$ is attributed to the LH-SLTJ

enabled spin-selective broad-band transmission as shown in Fig. 12(c).

G. Device characteristics of the Gaussian Height based Nu-SLTJ(GH-SLTJ)

To realize the Gaussian height(GH) based Nu-SLTJ shown in Fig. 4(b), we engineer the scattering potential

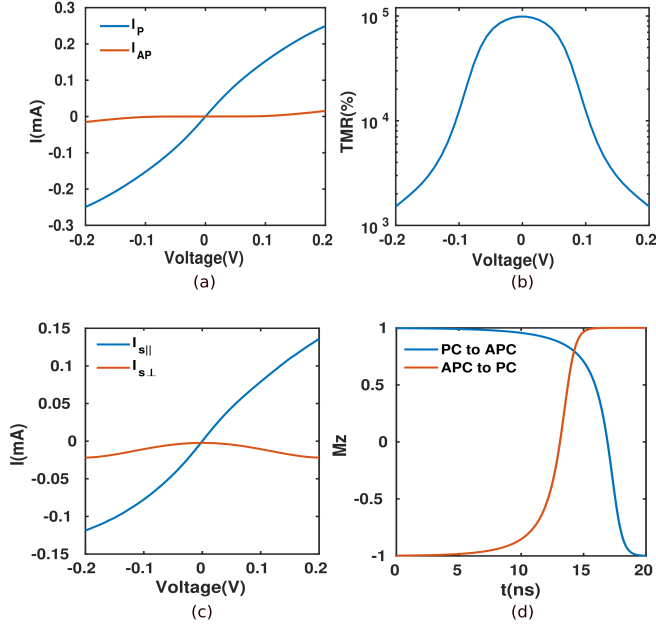


FIG. 13. (a) I-V characteristics of the GH-SLTJ in the PC(I_P) and APC(I_{AP}). (b) Variation of TMR(%), (c) $I_{s||}$ and $I_{s\perp}$ with the applied voltage. (d) STT based switching of the free layer from the PC to APC($V=-13.64$ mV) and the APC to PC($V=13.64$ mV).

($E_f + U_{Bn}$) of the n-th barrier in such a way that

$$E_f + U_{Bn} = (E_f + U_{B0})e^{-n^2/16}$$

where $SP_0 = E_f + U_{B0} = 3.01$ eV and $n=0,1,2$.

Figure 13(a) depicts the I-V characteristics of GH-SLTJ in the PC and the APC. The maximum TMR(%) we notice in this case is nearly $\approx 9.87 \times 10^4\%$ (Fig. 13(b)). In Fig. 13(c) we present the variation of the $I_{s||}$ and $I_{s\perp}$ with applied voltage. Fig. 13(d) describes the STT-switching of the free layer in the GH-SLTJ where the applied voltages for the PC to APC and the APC to PC switching are -13.64 mV and 13.64 mV, respectively. The SSB observed in this case is the 7th largest with 4.9 (see Tab. I). The significant improvement in the TMR(%) and $I_{s||}$ we achieve via GH-SLTJ can be elucidated in light of the heterostructure enabled broad-band spin filtering demonstrated by Figs. 19(c)&(d).

H. Device characteristics of the Nu-SLTJ with Lorentzian Height Profile(LRH-SLTJ)

We now advance to engineer the Lorentzian height(LRH) based Nu-SLTJ shown in Fig. 4(c), where the scattering potential($E_f + U_{Bn}$) of the n-th barrier in terms of the central barrier is given by

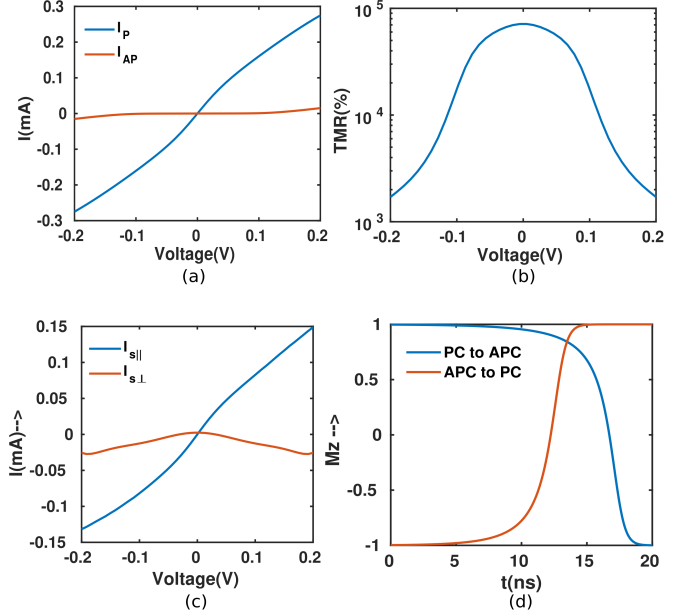


FIG. 14. (a) I-V characteristics of the LRH-SLTJ in the PC(I_P) and APC(I_{AP}). (b) Variation of TMR(%), (c) $I_{s||}$ and $I_{s\perp}$ with the applied voltage. (d) STT based switching of the free layer from the PC to APC($V=-12.3$ mV) and the APC to PC($V=12.3$ mV).

$$E_f + U_{Bn} = (E_f + U_{B0}) \frac{\Gamma^2}{n^2 + \Gamma^2}$$

with $\Gamma = 4$, $SP_0 = E_f + U_{B0} = 3.01$ eV and $n=0,1,2$.

In Fig. 14(a), we present the I-V characteristics of the LRHSLTJ in the PC and the APC. The maximum TMR(%) we observe in this case is close to $\approx 7.13 \times 10^4\%$ (Fig. 14(b)). Figure 14(d) describes the switching dynamics of the free layer with the $SB^{PC \rightarrow APC}$ and $SB^{APC \rightarrow PC}$ of -12.3 mV and 12.3 mV, respectively. Therefore, the LRH-SLTJ yields the 6th largest SSB with 5.4 (see Tab. I). The momentum enhancement in the TMR(%) and $I_{s||}$ (Fig. 14(c)) in the LRH-SLTJ can be reasoned out on the basis of the spin selective broad-band filtering demonstrated in Figs. 19(e)&(f).

I. Device Characteristics of the Nu-SLTJ with Pöschl Teller Height Profile(PH-SLTJ)

To devise the Pöschl Teller height based Nu-SLTJ shown in Fig. 4, we consider the scattering potential($E_f + U_{Bn}$) of the n-th barrier(b_n) as

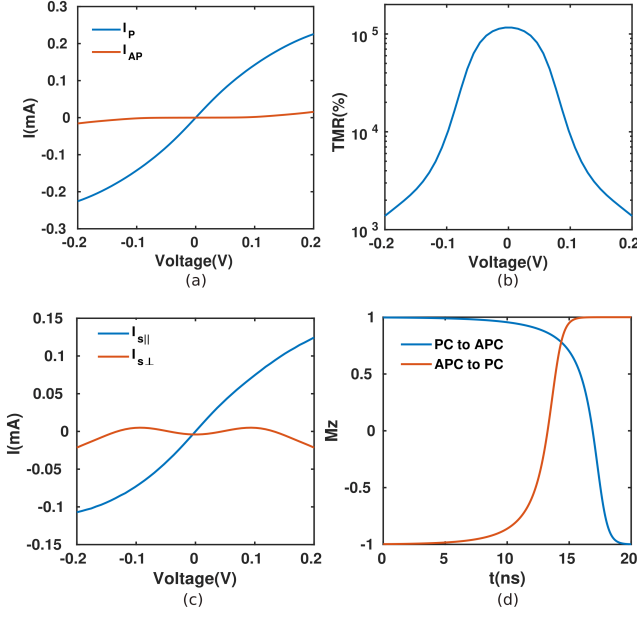


FIG. 15. (a) I-V characteristics of the PH-SLTJ in the PC(I_P) and APC(I_{AP}). (b) Variation of TMR(%), (c) $I_{s||}$ and $I_{s\perp}$ with the applied voltage. (d) STT based switching of the free layer from the PC to APC($V=-15$ mV) and the APC to PC($V=15$ mV).

$$E_f + U_{Bn} = (E_f + U_{B0}) \frac{2}{e^{n/4} + e^{-n/4}}$$

where $SP_0 = E_f + U_{B0} = 3.01$ eV and $n=0,1,2$.

In Fig. 15(a), we present the I-V characteristics of the PHSLTJ in the PC and the APC. The maximum TMR(%) provided by the device is nearly $\approx 1.16 \times 10^5\%$ (Fig. 15(b)). The variation of $I_{s||}$ and $I_{s\perp}$ with the applied voltage is plotted in Fig. 15(c). Figure 15(d) shows the STT-switching of the free layer from the PC to APC and the APC to PC with $SB^{PC \rightarrow APC}$ and $SB^{APC \rightarrow PC}$ of -15 mV and 15 mV, respectively. Thus, the PH-SLTJ provides the least SSB of 4.5 (see Tab. I). The large $I_{s||}$ and the towering TMR(%) we get to witness in the device can be explained on the basis of the spin-selective broad-band transmissions in the PC and the APC as shown in Figs. 19(g)&(h).

We also perform a comparative study of all these Nu-SLTJs along with a regular(R)-SLTJ (Fig. 2(b)) as shown in Fig. 6. In our simulations, we have taken the thickness of all the oxide layers and the scattering potentials of the R-SLTJ as 0.8 nm and 3.01 eV respectively.

IV. PERFORMANCE OF THE NU-SLTJS AT HIGHER VOLTAGES

Another significant aspect of the work regarding the Nu-SLTJs encircles their performance indices at higher voltages. Hitherto, the engineering of a robust TMR(%)

with the applied bias has appeared to be a major challenge in the novel literature[44] that reverberates while designing the Nu-SLTJs as well. Nevertheless, we demonstrate that the introduction of superlattices can accomplish a decent TMR(%) at a higher voltage and also explore the maximum achievable $I_{s||}$ via various Nu-SLTJs to perform faster switching.

In the first place, we present a qualitative overview of

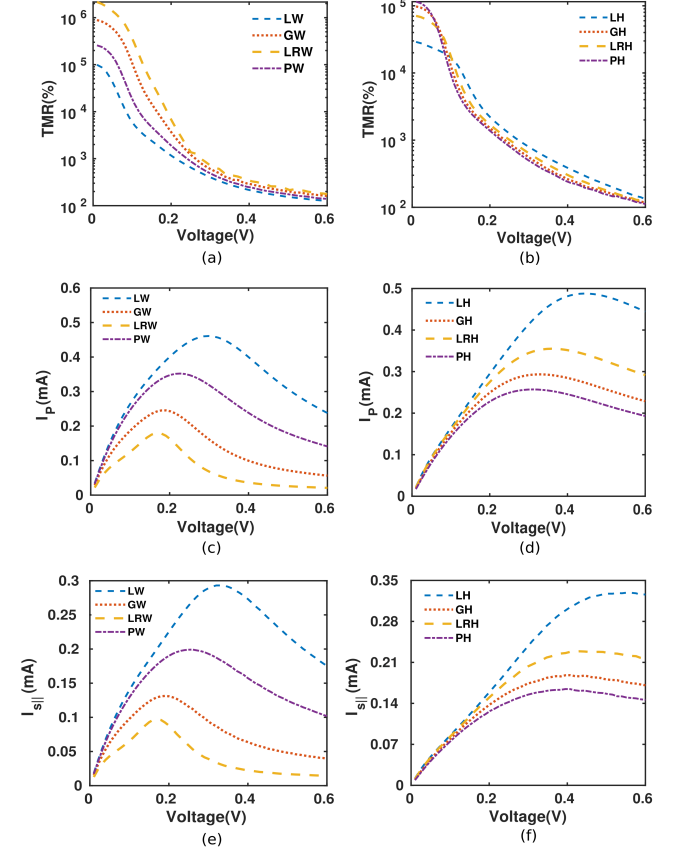


FIG. 16. High-voltage characteristics: Variation in the TMR(%) of the (a)W-SLTJs and the (b)H-SLTJs, charge current(I_P) of the (b)W-SLTJs and the (c)H-SLTJs and the $I_{s||}$ of the (e) W-SLTJs and the (f) H-SLTJs with respect to the applied bias.

the current flow through an Nu-SLTJ on the application of an applied bias, governed by the areas of the transmissions in the PC(A_{PC}) and APC(A_{APC}). To calculate the current for a specific voltage, we multiply the quantity $(f_F(E) - f_f(E))$ with the transmission $T(E)$, where the f_F and f_f represent the Fermi distribution functions of the fixed and free FMs, respectively. Along with an increase in the voltage across an Nu-SLTJ, the difference between the f_F and f_f goes up, resulting a greater leeway for tunneling of the electrons that leads to an upsurge in the current conduction. Besides, furtherance in the voltage after a certain point fails to engender an increment in the current flow. This can be ascribed to the bandpass nature of the transmission that inhibits any ad-

TABLE I. Performance indices of all the Nu-SLTJs, along with the R-SLTJ, and the AR-SLMTJ. Here $\text{TMR}(\%)^{Peak}$ denotes the maximum TMR(%) provided by a device, V_P represents the voltage where I_P peaks and $I_{s||}^{Peak}$ denotes the maximum achievable spin current. The quantities $\text{SB}^{PC \rightarrow APC}$ and $\text{SB}^{APC \rightarrow PC}$ represent the switching biases for the PC to APC and the APC to PC switching, respectively. $\text{TMR}(\%)_{V_P}$ indicates the TMR at V_P , and t^{FS} denotes the time required for the fastest switching.

| Type of Device | $\text{TMR}(\%)^{Peak}$ | $\text{SB}^{PC \rightarrow APC}$ (mV) | $\text{SB}^{APC \rightarrow PC}$ (mV) | SSB | V_P (V) | $\text{TMR}(\%)_{V_P}$ | $I_{s }^{Peak}$ (mA) | I_P^{Peak} (mA) | t^{FS} (ps) |
|----------------|-------------------------|---------------------------------------|---------------------------------------|------|-----------|------------------------|-----------------------|-------------------|---------------|
| MTJ | 240 | -74 | 60 | 1 | - | - | - | - | - |
| R-SLTJ | 1.44×10^5 | -20.4 | 20.4 | 3.28 | 0.24 | 6.24×10^2 | 0.103 | 0.17 | 1061 |
| LW-SLTJ | 1.01×10^5 | -7.4 | 7.4 | 9.05 | 0.3 | 4.06×10^2 | 0.3 | 0.47 | 380 |
| GW-SLTJ | 9.01×10^5 | -8.88 | 8.88 | 7.61 | 0.19 | 4.7×10^3 | 0.13 | 0.25 | 882 |
| LRW-SLTJ | 2.19×10^6 | -11.7 | 11.7 | 5.73 | 0.18 | 1.53×10^4 | 0.1 | 0.18 | 1158 |
| PW-SLTJ | 2.61×10^5 | -7.75 | 7.75 | 8.7 | 0.22 | 1.24×10^3 | 0.2 | 0.35 | 563 |
| LH-SLTJ | 2.9×10^4 | -11.6 | 11.6 | 5.8 | 0.43 | 3.18×10^2 | 0.33 | 0.49 | 355 |
| GH-SLTJ | 9.87×10^4 | -13.64 | 13.64 | 4.9 | 0.31 | 5×10^3 | 0.19 | 0.3 | 621 |
| LRH-SLTJ | 7.13×10^4 | -12.3 | 12.3 | 5.4 | 0.36 | 4×10^2 | 0.22 | 0.35 | 508 |
| PH-SLTJ | 1.16×10^5 | -15 | 15 | 4.5 | 0.29 | 5.6×10^2 | 0.16 | 0.26 | 672 |
| ARSLMTJ[43] | 3×10^4 | -12 | 12 | 5.6 | 0.088 | 9.8×10^3 | 0.06 | 0.9 | 1996 |

ditional area of the transmission(A_T) from falling within the Fermi window(FW) beyond an instance when the FW engulfs significant A_T . Moreover, as the magnitude of the applied voltage is increased even further, the transmission spectrum of a typical Nu-SLTJ becomes tapered. This results in a reduction in the current conduction that compels all the Nu-SLTJs to exhibit negative differential resistance(NDR) beyond a specific voltage(V_P).

We present the high-voltage characteristics of various Nu-SLTJs in Fig. 16 and show the variation of the TMR(%), $I_{s||}$ and the I_P while varying the applied voltage from 0.01 V to 0.6 V. We exclude the point at $V=0$, where the TMR of the devices becomes immeasurable owing to the zeroed I_P and I_{AP} . In Fig. 16(a),(b),(c)&(d) we show that the TMR of both the H-SLTJs and the W-SLTJs exhibits a large variation with respect to the applied bias alongside an NDR of the I_P -V characteristics after V_P . Interestingly, after reaching the peak, the decline in the $I_{s||}$ of the H-SLTJs as shown in Fig. 16(e)&(f) becomes nearly insignificant, thereby providing grist to an idea for utilizing this behavior to realize a device that produces invariable $I_{s||}$ with an applied voltage.

The deterioration in the ratio of A_{PC} and A_{APC} quenches the TMR(%) of an orthodox MTJ at a higher voltage. For instance, the trilayer MTJ we present in this work offers a TMR(%) of $\approx 220\%$ and $\approx 140\%$ at an applied voltage of 10 mV and 300 mV as shown in Fig. 7(b). We stumble upon a similar problem while engineering the Nu-SLTJs as well. Yet, the heterostructure-enabled broad-band spin filtering inhibits the TMR(%) from falling below $\approx 10^3$ - 10^4 (%) while the applied bias ranges from -0.2V-0.2V. This provides a decent solution regarding the sensitivity of the MTJs within this range. Another question, that may lie dormant is the importance of the TMR(%) at a higher voltage while the switching biases of all the SLTJs lie fairly below 50 mV, which is answered by highlighting the applicability of an MTJ in the STNOs. A high TMR(%) at V_P offers a big-

ger difference between the I_P and I_{AP} , which ensures a surge in the microwave output power. Therefore the Nu-SLTJs, while providing a far superior TMR(%) and I_P compared to an MTJ, emerge as more suitable alternatives in order to design large frequency STNOs with high microwave output power[31]. Furthermore, we can infer from Tab. I that the LW-SLTJ provides an I_P of 0.47 mA at the V_P along with a TMR(%) of 4.06×10^2 (%) which entitles the device as a much coveted candidate for the aforementioned application.

V. COMPARISON OF THE PERFORMANCE INDICES OF THE VARIOUS NU-SLTJS

In this section, we discuss the performance indices of the various SLTJs presented in Tab. I and carry out a comparative study in reference to the transmission profiles described in Appendix B. We attribute the monumental TMR(%) profiles accomplished via different heterostructures to the towering ratio of the transmissions in the PC(T_{PC}) and APC(T_{APC}), and elucidate the significant enhancement in the $I_{s||}$ by the spin selective nature of the broad-band T_{PC} (see Appendix B).

Figure. 17 exemplifies that the LW-SLTJ yields the largest T_{PC} and hence offers a sizeable $I_{s||}$ that leads to the highest SSB (see Tab. I) among all the Nu-SLTJs. Thereafter, the PW-SLTJ, GW-SLTJ and LRW-SLTJ comprise the list of the W-SLTJs in the descending order with reference to the A_{PC} as shown in Fig. 17. A similar order of the $I_{s||}$ and SSB of the respective W-SLTJs corroborates the potential impact of the A_{PC} on the Slonczewski term($I_{s||}$). We also get to witness an impressive consistency in the order of the TMR(%) with the ratio of the A_{PC} and A_{APC} while analysing the relative performances of the various W-SLTJs. Fig. 17 conveys the LRW-SLTJ to possess the largest A_{PC}/A_{APC} which enables the device to exhibit the tallest TMR(%). Inter-

estingly, the ascending order of the W-SLTJs with respect to the $I_{s||}$ constitutes the descending order with reference to the TMR(%).

Akin to the W-SLTJs, the heterostructure-enabled spin-selective transmissions play a significant role in governing the performance indices of the H-SLTJs as well. The LH-SLTJ, LRH-SLTJ, GH-SLTJ, and PH-SLTJ comprise the descending order of the H-SLTJs with respect to the A_{PC} as shown in Fig. 19. The $I_{s||}$ we observe in these devices are congruent with their transmission spectra. For instance, the GH-SLTJ yields an exacerbated T_{PC} compared to the LH-SLTJ resulting in a decimated $I_{s||}$. In addition to this, we also find the variation in the TMR(%) to be proportional with the ratio of A_{PC} and A_{APC} . As we move from the PH-SLTJ to LH-SLTJ, the depression in the value of A_{PC}/A_{APC} reduces the magnitude of the TMR(%). Similar to the W-SLTJs, the order of the H-SLTJs with respect to $I_{s||}$ and TMR(%) are mutually opposite.

It seems pretty outlandish that despite having a significant T_{PC} , the H-SLTJs tend to fall behind in accomplishing a mammoth SSB, unlike the W-SLTJs. We can ascribe such behaviour to the widespread finger-like profile of the transmissions (see Fig 17 & 19), which reduces effective area within the Fermi window near the switching bias and scales down the steepness of the $I_{s||}$ -V characteristics (see Fig. 16(e)&(f)). On the contrary, although the W-SLTJs exploits their compact T_{PC} to accomplish a sharp slope in the $I_{s||}$ -V curve, the narrower width in the T_{PC} reduces the V_P of the devices. As a consequence, the W-SLTJs tend to exhibit the NDR at a lower voltage.

The compendium of Nu-SLTJs devised in this work offer fairly superior performances compared to the anti-reflective superlattice magnetic tunnel junction (AR-SLMTJ) [43] in many ways. In the first place, we can infer from Tab. I that the SSB of the ARSLMTJ is lower than that of all the W-SLTJs, including the LH-SLTJ. Other than that, the maximum $I_{s||}^{peak}$ and the TMR_{V_P} that we accomplish via LH-SLTJ and LRW-SLTJ are 600% and 150% higher than same. Importantly, both the W-SLTJs and the H-SLTJs may comprise minimal device structures of three oxide barriers (see Fig. 6) whereas the ARSLMTJ requires minimum five barriers for operation. Thus, the resounding superiority in the performance indices takes place in the Nu-SLTJs along with reduction in fabrication complexity.

It is worth mentioning that despite having a near box-cart transmission, the ARSLMTJ fails to outperform the W-SLTJs and the LH-SLTJ while providing a lower SSB. This can be accounted to the narrowness of its transmission, which reduces the A_{PC} engulfed by the FW near the switching bias. These findings do not underpin the necessity of the box-cart-shaped transmissions and establish the importance of a higher A_{PC} within the FW as the keystone for accomplishing a lower switching bias. Another dimension that we unveil in this work is the high TMR(%) (Fig. 6(a)&(b)) of the R-SLTJ de-

void of a box-cart T_{PC} (Fig. 20(c)), which demonstrates the A_{PC}/A_{APC} to be the predominant factor in order to achieve a high TMR(%).

VI. CONCLUSION

Low TMR(%) and high switching bias [31–33] are the two foremost drawbacks that gridlock the possibility a typical MTJ to become a superior alternative for state-of-the-art storage devices. This study explores the broadband spin filtering in various Nu-SLTJs that manifests an appreciable enhancement in the TMR and a significant SSB, while endowing the LW-SLTJ with the best TMR(%)– $I_{s||}$ trade-off ($TMR(\%) \approx 10^5$, $SSB \approx 9.05$ and $t^{FS} \approx 380$ ps). Since the Nu-SLTJs accomplish a fast STT-switching in the order of a few hundreds of picoseconds, they successfully address the shortcoming of non-deterministic switching in the SOT devices while keeping up with the speed [27]. We unveil that a large A_{PC} and a high A_{PC}/A_{APC} within the FW overrides the necessity for the box-cart shape of a transmission in order to obtain a low switching bias and a high TMR(%). Apart from that, we anticipate the Nu-SLTJs devised to find possible applications in the STNOs due to their large I_P and considerable TMR(%) at V_P . Moreover, we foresee the recent development of double metallic quantum well based MTJs [36] to add further fuel in the investigation of heterostructure based memory devices. Finally, we conclude the theoretical analysis of Nu-SLTJs with lower switching bias and high TMR(%) proposed in this article to hopefully pave the avenues for cutting-edge heterostructure-based magnetic tunnel junctions.

ACKNOWLEDGEMENTS

The author AS acknowledges the support of ISIRD phase-1 project of IIT Ropar.

DATA AVAILABILITY STATEMENT

The data that support the findings of this study are available upon reasonable request from the authors

Appendix A: Switching of the free layer

This section deals with the STT-switching of the free FM in the LW-SLTJ, as shown in Fig. 18. The analysis of the switching dynamics involves the self-consistent coupling of the NEGF formalism with the LLGS equation described in Fig. 5. As the applied $I_{s||}$ and the magnetisation of the free FM resides in the same direction at equilibrium, it is necessary to impart a slight misalignment in the magnetisation to produce a non-zero torque [27]. Since, it is not possible to switch the free FM

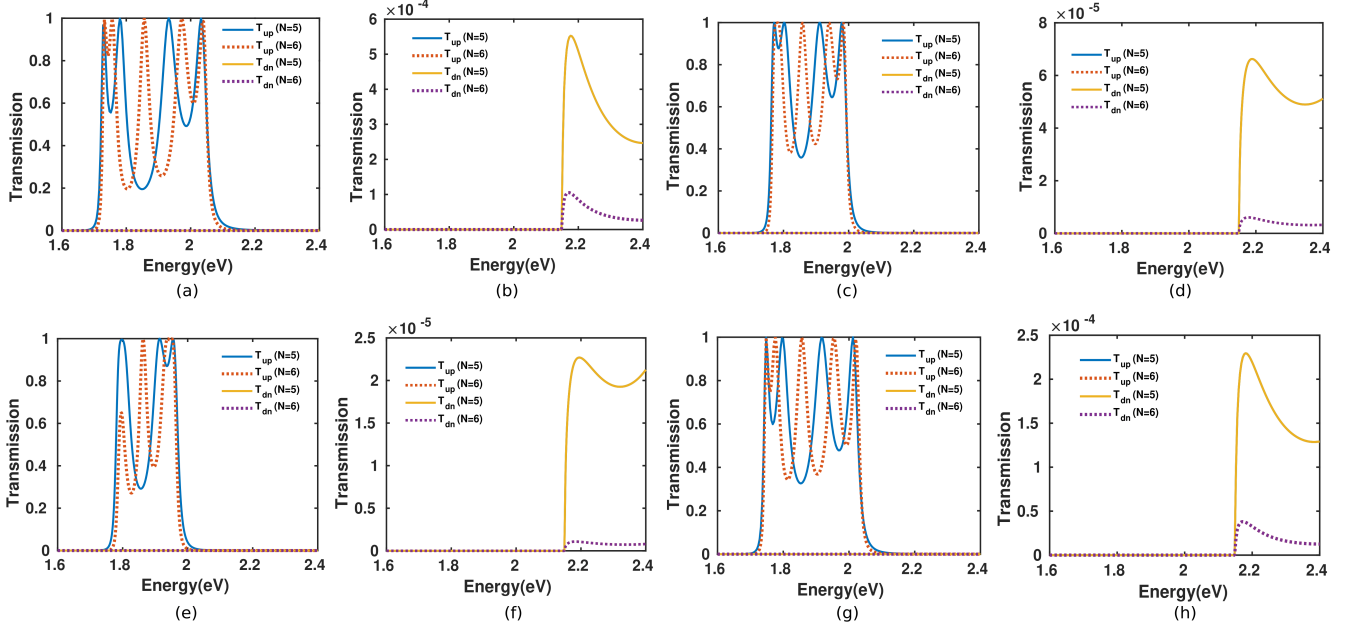


FIG. 17. Transmission profiles of the (a) LW-SLTJ in the PC and (b) the APC, (c) GW-SLTJ in the PC and (d) the APC, (e) LRW-SLTJ in the PC and (f) the APC (g) PW-SLTJ in the PC and (h) the APC at the lowest available transverse energy with an applied bias of $V=0V$. Here T_{up} denotes up-spin transmission and T_{dn} represents down-spin transmission. The transmissions are given for number of oxide barriers(N)=5 and $N=6$.

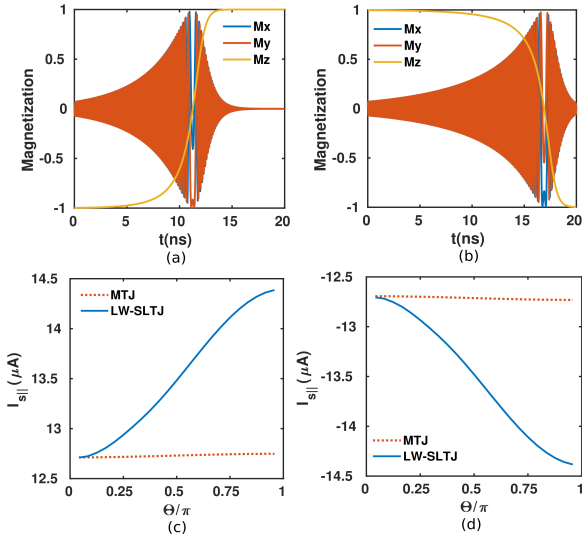


FIG. 18. Switching dynamics of the LW-SLTJ: (a) APC to PC switching ($V=7.4$ mV) (b) PC to APC switching ($V=-7.4$ mV). Variation of the $I_{s||}$ with θ for the LW-SLTJ(MTJ) at (c) $SB_{LW-SLTJ(MTJ)}^{APC \rightarrow PC}$ and (d) $SB_{LW-SLTJ(MTJ)}^{PC \rightarrow APC}$.

from either 0° or 180° for the above mentioned reasons, we assume the relative angle between the magnetisation of the free and the fixed FM(Θ) as 4° and 176° in the PC and the APC, respectively. Apart from that, a switching current near the $I_{s||,c}$ induces an insignificant damping to the magnetization. Hence in order to perform a comfort-

able switching, we apply an $I_{s||}$ that exceeds the critical current $I_{s||,c}$ by 20%. The desired $I_{s||}$ is achieved with an $SB_{PC \rightarrow APC}^{PC \rightarrow APC}$ and $SB_{APC \rightarrow PC}^{APC \rightarrow PC}$ of -7.4 mV and 7.4 mV, respectively. In contrast to an typical MTJ, we observe a considerable variation in the $I_{s||}$ of the LW-SLTJ with respect to the Θ as shown in Fig. 18(c)&(d). Therefore, the time required for the PC to APC(Fig. 18(a)) and the APC to PC(Fig. 18(b)) switching becomes dissimilar. Analogous to the LW-SLTJ, the $I_{s||}$ of all the Nu-SLTJs devised in this work exhibit a similar behavior with the Θ . The magnitude of the $SB_{PC \rightarrow APC}^{PC \rightarrow APC}$ and the $SB_{APC \rightarrow PC}^{APC \rightarrow PC}$ remains the same for all the Nu-SLTJs due to symmetrical variation of the $I_{s||}$ with respect to the applied voltage near 0V.

Appendix B: Analysis of the Transmission Spectra

The analysis of the transmission spectra provide vivid insights to engineer the heterostructure based magnetic tunnel junctions. In order to determine the current through a mesoscopic device such as an MTJ and/or Nu-SLTJ, we multiply the fermi level difference of the fixed and free FMs to the transmission and integrate the product over the energy. Hence, the ratio of the A_{PC} and A_{APC} within the fermi-window (FW) plays a pivotal role in governing the TMR(%). Apart from that, the up-spin transmission(T_{up}) in a spin selective heterostructure heavily dominates its down-spin counterpart(T_{dn}). Such compelling spin filtering causes the spin($I_z = I_{up} - I_{dn}$) and

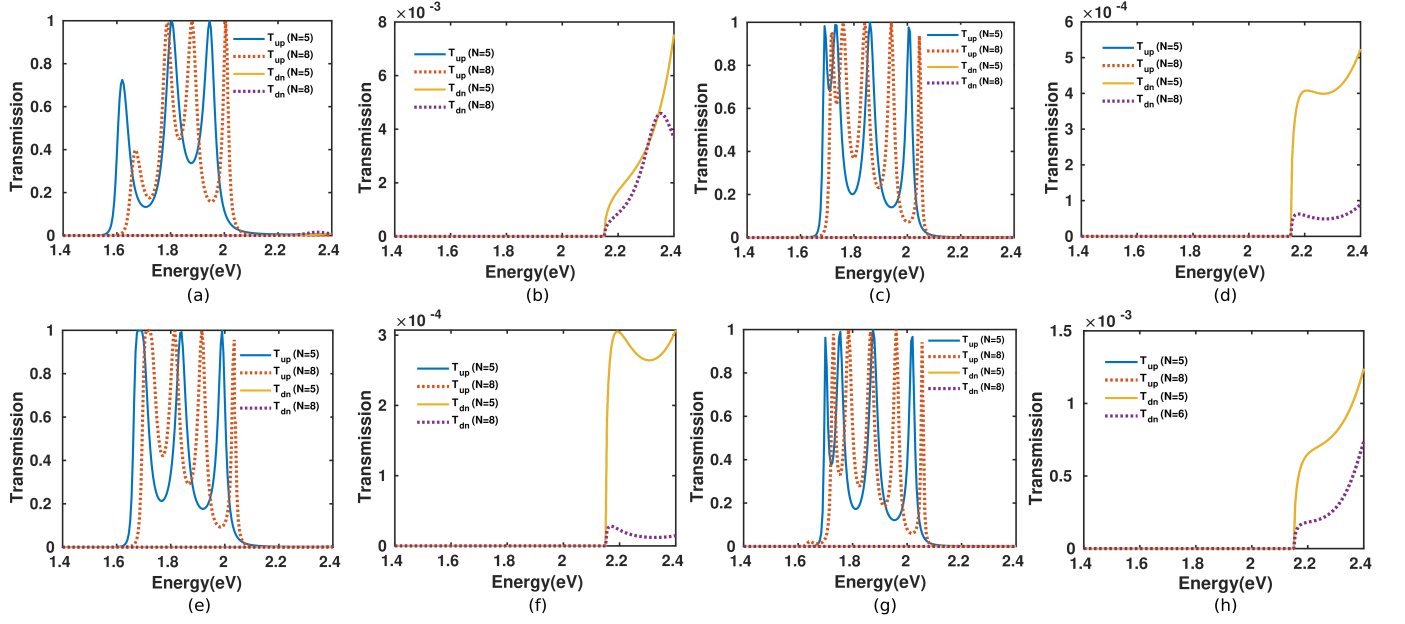


FIG. 19. Transmission profile: (a) LH-SLTJ in the PC and (b) APC, (c) GH-SLTJ in the PC and (d) APC, (e) LRH-SLTJ in the PC and (f) APC, (g) PH-SLTJ in the PC and (h) APC at the lowest available transverse energy with an applied bias of $V=0V$. Here T_{up} denotes upspin transmission and T_{dn} represents downspin transmission. The transmissions are given for the number of oxide barriers(N)=5 and $N=6$.

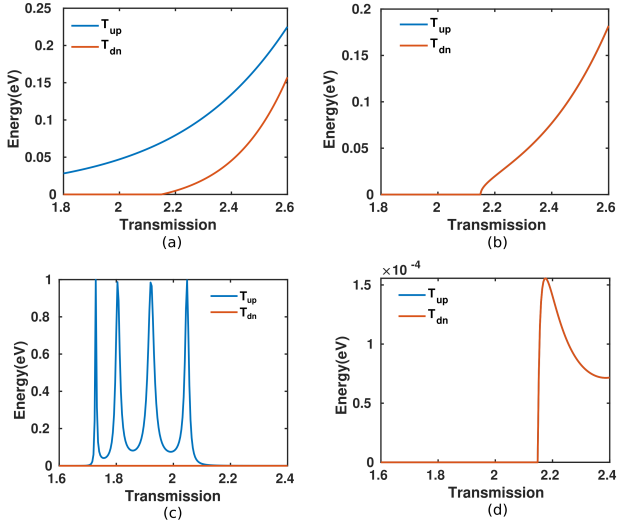


FIG. 20. (a) Transmission profile of the trilayer MTJ in the PC and (b) APC, (c) transmission profile of the R-SLTJ in the PC and (b) APC at the lowest available transverse energy(E_t) with the applied voltage $V=0V$. Here T_{up} denotes upspin transmission and T_{dn} represents downspin transmission.

the charge current(I_P) in the z direction to become nearly equal in magnitude. Further, the strong correlation of the I_z with the Slonczewski term ($I_{s||}$) in the spin selective SLTJs ensures a high I_P to eventuate a large $I_{s||}$. Based on this heuristic arguments, we utilize the T_{PC} to predict the behavior of the $I_{s||}$ with the applied bias.

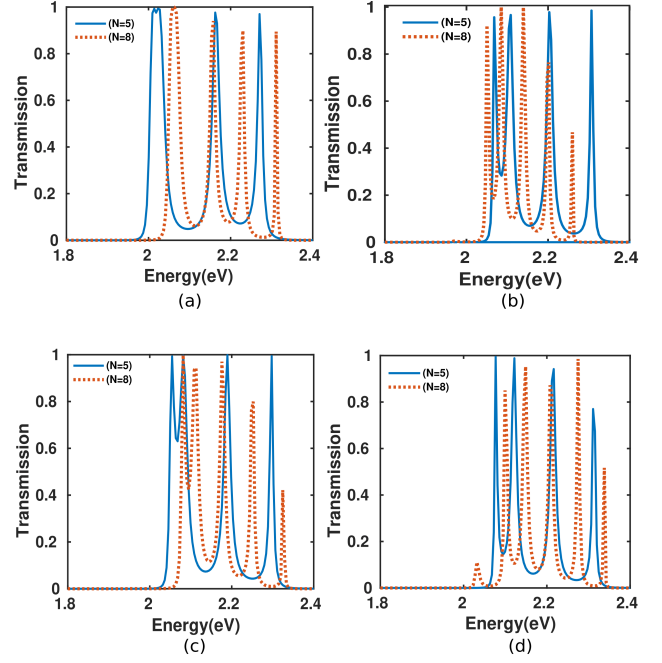


FIG. 21. Transmission profiles of the (a) LH-SLTJ, (b) GH-SLTJ, (c) LRH-SLTJ and (d) PH-SLTJ in the PC for $N=5$ and $N=8$ at an $E_t=0.2$ eV with the applied voltage $V=0$.

We embark on elucidating the spintronic characteristics of various Nu-SLTJs with the T_{PC} and T_{APC} of both the trilayer MTJ and the regular SLTJ depicted in Fig.

20. The modest opposite spin transmission shown in Fig. 20(a) declines the spin filtering capability of the trilayer MTJ, which restricts the TMR to a trifling 240% compared to the Nu-SLTJs. In addition to this, the value of the T_{PC} lies well below 1 within the FW which exacerbates the A_{PC} resulting in a low $I_{s||}$. On the other hand, despite offering a commendable spin filtering, the R-SLTJ exhibits a finger like T_{PC} which significantly reduces the A_{PC} and thereby yields a feeble $I_{s||}$ along with a meager SSB. Therefore, we propose the idea of Nu-SLTJs, where the presence of the electronic Bloch states in the neighbourhood of the resonant peaks gives rise to a spin selective broad-band T_{PC} , resulting an admirable $I_{s||}$. The broad-band spin filtering is referred to the widened T_{PC} that allows a broad transmission window for the electrons aligned to the FMs in the PC, while the opposite spin transmission is nearly suppressed to zero as shown in Figs. 19,17. Further, the towering ratio of the A_{PC} and the A_{APC} witnessed in the Nu-SLTJs (Figs. 19,17) leads to an ultra-high boost in the TMR(%).

In Fig. 17 we present the transmissions of various W-SLTJs in the PC and the APC for both $N = 5$ and $N = 6$, where N denotes the number barriers comprising the Nu-SLTJs. We find the quantity A_{PC}/A_{APC} and the T_{PC} to elucidate the TMR(%) and the $I_{s||}$ with a noble consistency. For example, the ratio of the A_{PC} and A_{APC} is able to coherently predict the comparative performance of the TMR(%) in the various W-SLTJs. In addition to this, the relative magnitude of the $I_{s||}$ corroborates the decisive impact of the T_{PC} on it. Regardless of the width based profiles, the passband in the T_{PC} exhibits remnant oscillations as described in Fig. 17. The T_{PC} of the W-SLTJs display a slight reduction in the area with a surge in the oscillations as the number of barriers are increased from $N = 5$ to $N = 6$. Fig. 6(a) shows a steep upsurge in the TMR(%) as we increase the number of barriers from five to six which can be categorically explained by the sharp dip in the A_{APC} at $N = 6$ as depicted in Fig. 17. At the same time, the comparable $I_{s||}$ of the LW-SLTJ, GW-SLTJ and the PW-SLTJ at $N = 5$ and $N = 6$ maintain a precise consistency with their T_{PC} . The considerable reduction in the A_{PC} of the LRW-SLTJ from $N = 5$ to $N = 6$ reverberates in its $I_{s||}$ as well.

In Fig. 19, we show both the T_{PC} and T_{APC} of all the H-SLTJs for $N = 5$ and $N = 8$. We find H-SLTJs display more intricate results in comparison to their width based counterparts. As we increase the number of the barriers from $N = 5$ to $N = 8$, even though the A_{PC} of the GH-SLTJ, LRH-SLTJ, and the PH-SLTJ shows an upsurge, the $I_{s||}$ of the respective devices suffers a decline in contrast to our earlier discussion. This might appear to be a clear dichotomy in the first place but we find the explanation of the bewilderment to be concealed behind the transmissions at higher transverse modes(E_t)[43]. As we move towards higher E_t , the gross bulk of a transmission spectra approaches the Fermi window and then eventually moves beyond it. Hence the transmissions at a higher

E_t around the fermi window plays a more conclusive role in order to determine the $I_{s||}$ and the TMR(%). In Fig. 21(b),(c)&(d) we demonstrate that for $E_t = 0.2$ eV the A_{PC} of the GH-SLTJ, LRH-SLTJ, and the PH-SLTJ at $N = 5$ offers a higher area than that of at $N = 8$, thereby drawing a coherent conclusion in this regard. Apart from that, the increase in the TMR(%) of the H-SLTJs from $N = 5$ to $N = 8$ is clearly interpretable from Fig. 19.

Appendix C: Guidelines for Designing the Nu-SLTJs

In this leg of the article, we describe the impact of modulating the scattering potential(SP) and width(b) of the

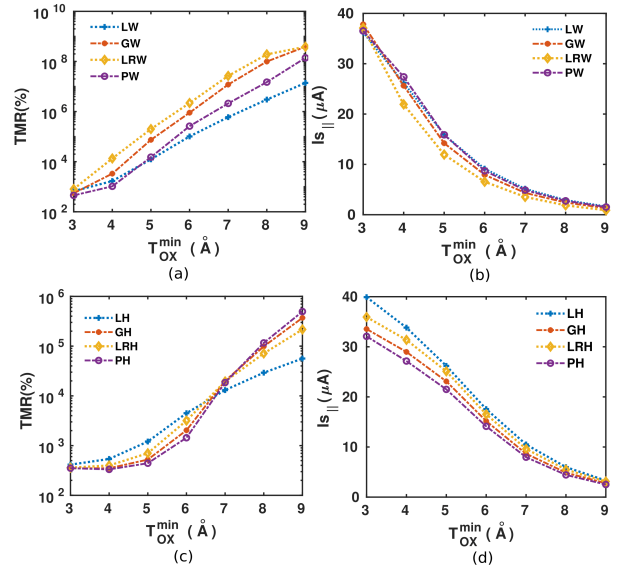


FIG. 22. Device characteristics: The variation in the TMR(%) of the (a)W-SLTJs and the (b)H-SLTJs, $I_{s||}$ of the (c)W-SLTJs and the (d)H-SLTJs with the T_{OX}^{min} at an applied bias of $V = 5$ mV.

oxide barriers to design the Nu-SLTJs and argue that altering either of them for enhancing the TMR(%) abates the $I_{s||}$ and vice versa, thereby leading to a novel hypothesis of TMR- $I_{s||}$ trade off. In Fig. 22 we present the variation of the TMR and $I_{s||}$ while varying the minimum thickness of the oxide layer of Nu-SLTJs from 3Å to 9Å. Besides T_{OX}^{min} determines the thickness of all the other barriers in the W-SLTJs, the thickness of each barriers comprising an H-SLTJ is T_{OX}^{min} itself. The results we obtain from Fig.22 demonstrate that an increase in the T_{OX}^{min} eventuates a near monotonic upsurge of the TMR while manifesting an opposite impact on the $I_{s||}$. We may attribute such behavioral pattern to the fact that a wider T_{OX} bestows an exacerbated A_{PC} resulting a decimated $I_{s||}$, and at the same time boosts the ratio of the A_{PC} and A_{APC} leading to an increase in the TMR. Analogously, we also perform the analysis regarding the

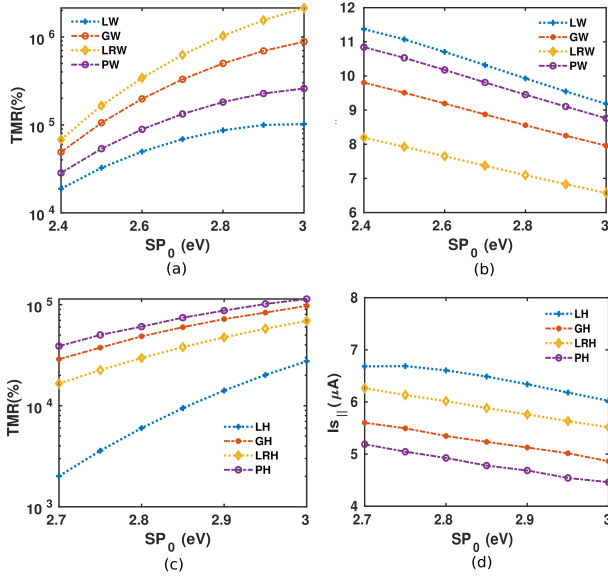


FIG. 23. Device characteristics: The variation in the TMR(%) of the (a)W-SLTJs and the (b)H-SLTJs, $I_{s||}$ of the (c)W-SLTJs and the (d)H-SLTJs with the SP_0 at an applied voltage of $V=5$ mV.

impact of varying scattering potentials(SP) of the oxide barriers on the H-SLTJ and demonstrate the behavior of the $I_{s||}$ and the TMR to be entangled in a similar fashion.

On the similar lines, we vary the SP s of the W-SLTJs from 2.4 eV to 3 eV and depict the device characteristics in Fig. 23(a)&(b). Since the SP of the terminal barriers(SP_{tb}) depends on the central barrier(SP_0) in the H-SLTJs, lowering the SP_0 significantly reduces the height of the SP_{tb} far below the Fermi energy, thereby sabotaging the spin filtering near the FW. To avoid this muddle, we keep the variation of the SP_0 within the limits of 2.7 eV to 3 eV for studying the characteristics of the $I_{s||}$ and the TMR as shown in Fig 23(c)&(d). The results we obtain in this context conveys that an increase in the scattering potential reduces the $I_{s||}$ and improves

the TMR which may again be attributed to the reduction in the A_{PC} and improvement in the ratio of the A_{PC} and A_{APC} , respectively. A qualitative analysis of Fig. 22 and Fig. 23 reveal that the change in the width of the oxide barriers elicit more pronounced impact on the TMR and the $I_{s||}$ among the SLTJs compared to the variation in the height of the SP s. Therefore, we may use the variation of the T_{OX} to design the framework of a Nu-SLTJ, while the alteration in the scattering potential might come handy during the fine-tuning of the performance indices.

The algorithm described in Fig. 24, presents a generic guideline to modulate the performance indices of a typical Nu-SLTJ in order to optimize it for various applications. While using the minimum number of oxide layers to moderate the fabrication complexity, a designer is left to alter only with the thickness of the oxide layers and

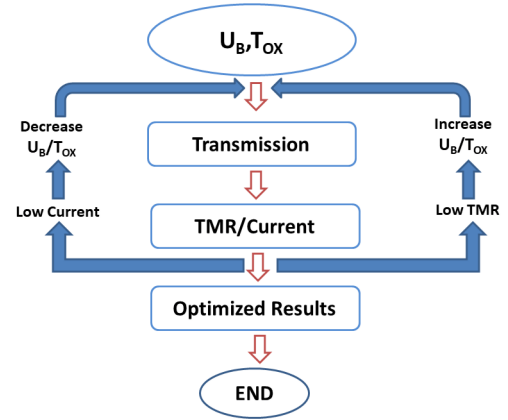


FIG. 24. Optimization Algorithm

the scattering potential of the insulators as the U_{BW} is fixed for a particular NM and the width of the quantum well(W) is decided beforehand for the optimization purposes[44]. Therefore, by following the algorithm depicted in Fig. 24 one may play around with both the SP and T_{ox} to meet the target specifications.

- [1] S. S. Parkin, C. Kaiser, A. Panchula, P. M. Rice, B. Hughes, M. Samant, and S.-H. Yang, *Nature materials* **3**, 862 (2004).
- [2] L. Berger, *Physical Review B* **54**, 9353 (1996).
- [3] J. C. Slonczewski, *Journal of Magnetism and Magnetic Materials* **159**, L1 (1996).
- [4] K. Le Phan, H. Boeve, F. Vanhelfmont, T. Ikink, F. De Jong, and H. De Wilde, *Sensors and Actuators A: Physical* **129**, 69 (2006).
- [5] A. Kanno, N. Nakasato, M. Oogane, K. Fujiwara, T. Nakano, T. Arimoto, H. Matsuzaki, and Y. Ando, *Scientific reports* **12**, 1 (2022).
- [6] L. I. Rudin and S. K. Bramble, *Investigative Image Processing* **2942** (1997).
- [7] T. Chen, R. K. Dumas, A. Eklund, P. K. Muduli, A. Houshang, A. A. Awad, P. Dürrenfeld, B. G. Malm, A. Rusu, and J. Åkerman, *Proceedings of the IEEE* **104**, 1919 (2016).
- [8] P. Braganca, B. Gurney, B. Wilson, J. Katine, S. Maat, and J. Childress, *Nanotechnology* **21**, 235202 (2010).
- [9] D. Robbes, *Sensors and Actuators A: Physical* **129**, 86 (2006).
- [10] I. Krivorotov, N. Emley, J. Sankey, S. Kiselev, D. Ralph, and R. Buhrman, *Science* **307**, 228 (2005).
- [11] H. S. Choi, S. Y. Kang, S. J. Cho, I.-Y. Oh, M. Shin, H. Park, C. Jang, B.-C. Min, S.-I. Kim, S.-Y. Park, *et al.*, *Scientific reports* **4**, 1 (2014).
- [12] R. Cheng, D. Xiao, and A. Brataas, *Physical review letters* **116**, 207603 (2016).

- [13] N. Bhattacharjee, A. Sapozhnik, S. Y. Bodnar, V. Y. Grigorev, S. Y. Agustsson, J. Cao, D. Dominko, M. Obergfell, O. Gomonay, J. Sinova, *et al.*, Physical review letters **120**, 237201 (2018).
- [14] Y. Jiang, T. Nozaki, S. Abe, T. Ochiai, A. Hirohata, N. Tezuka, and K. Inomata, Nature materials **3**, 361 (2004).
- [15] S. Mangin, D. Ravelosona, J. Katine, M. Carey, B. Terris, and E. E. Fullerton, Nature materials **5**, 210 (2006).
- [16] Z. Diao, Z. Li, S. Wang, Y. Ding, A. Panchula, E. Chen, L.-C. Wang, and Y. Huai, Journal of Physics: Condensed Matter **19**, 165209 (2007).
- [17] T. S. Santos, G. Mihajlović, N. Smith, J.-L. Li, M. Carey, J. A. Katine, and B. D. Terris, Journal of Applied Physics **128**, 113904 (2020).
- [18] S. Ikeda, J. Hayakawa, Y. M. Lee, F. Matsukura, Y. Ohno, T. Hanyu, and H. Ohno, IEEE Transactions on Electron Devices **54**, 991 (2007).
- [19] D. Apalkov, A. Khvalkovskiy, S. Watts, V. Nikitin, X. Tang, D. Lottis, K. Moon, X. Luo, E. Chen, A. Ong, *et al.*, ACM Journal on Emerging Technologies in Computing Systems (JETC) **9**, 1 (2013).
- [20] A. Khvalkovskiy, D. Apalkov, S. Watts, R. Chepulsii, R. Beach, A. Ong, X. Tang, A. Driskill-Smith, W. Butler, P. Visscher, *et al.*, Journal of Physics D: Applied Physics **46**, 074001 (2013).
- [21] S. Bhatti, R. Sbiaa, A. Hirohata, H. Ohno, S. Fukami, and S. Piramanayagam, Materials Today **20**, 530 (2017).
- [22] S. Bonetti, V. Tiberkevich, G. Consolo, G. Finocchio, P. Muduli, F. Mancoff, A. Slavina, and J. Åkerman, Physical review letters **105**, 217204 (2010).
- [23] P. Villard, U. Ebels, D. Houssameddine, J. Katine, D. Mauri, B. Delaet, P. Vincent, M.-C. Cyrille, B. Viala, J.-P. Michel, *et al.*, IEEE Journal of solid-state circuits **45**, 214 (2009).
- [24] Z. Zeng, G. Finocchio, and H. Jiang, Nanoscale **5**, 2219 (2013).
- [25] K. Mizushima, K. Kudo, T. Nagasawa, and R. Sato, Journal of Applied Physics **107**, 063904 (2010).
- [26] W. Butler, X.-G. Zhang, T. Schulthess, and J. MacLaren, Physical Review B **63**, 054416 (2001).
- [27] A. Meo, J. Chureemart, R. W. Chantrell, and P. Chureemart, Scientific reports **12**, 1 (2022).
- [28] J. Slaughter, K. Nagel, R. Whig, S. Deshpande, S. Aggarwal, M. DeHerrera, J. Janesky, M. Lin, H.-J. Chia, M. Hossain, *et al.*, in *2016 IEEE International Electron Devices Meeting (IEDM)* (IEEE, 2016) pp. 21–5.
- [29] T. Endoh, H. Honjo, K. Nishioka, and S. Ikeda, in *2020 IEEE Symposium on VLSI Technology* (IEEE, 2020) pp. 1–2.
- [30] J. Byun, D.-H. Kang, and M. Shin, AIP Advances **11**, 015035 (2021).
- [31] A. Sharma, A. A. Tulapurkar, and B. Muralidharan, Phys. Rev. Applied **8**, 064014 (2017).
- [32] A. Sharma, A. Tulapurkar, and B. Muralidharan, IEEE Transactions on Electron Devices **63**, 4527 (2016).
- [33] A. Sharma, A. A. Tulapurkar, and B. Muralidharan, AIP Advances **8**, 055913 (2018).
- [34] C. Chen and W. Hsueh, Applied Physics Letters **104**, 042405 (2014).
- [35] C. H. Chen, Y. H. Cheng, and W. J. Hsueh, EPL (Europhysics Letters) **111**, 47005 (2015).
- [36] B. Tao, C. Wan, P. Tang, J. Feng, H. Wei, X. Wang, S. Andrieu, H. Yang, M. Chshiev, X. Devaux, *et al.*, Nano Letters **19**, 3019 (2019).
- [37] M. Bhattacharjee, H. Nemade, and D. Bandyopadhyay, in *Journal of Physics: Conference Series*, Vol. 759 (IOP Publishing, 2016) p. 012051.
- [38] P. Tseng, Z.-Y. Chen, and W.-J. Hsueh, New Journal of Physics **22**, 093005 (2020).
- [39] E. Diez, I. Gómez, F. Dominguez-Adame, R. Hey, V. Bellani, and G. Parravicini, Physica E: Low-dimensional Systems and Nanostructures **7**, 832 (2000).
- [40] I. Gómez, F. Dominguez-Adame, E. Diez, and V. Bellani, Journal of Applied Physics **85**, 3916 (1999).
- [41] A. Sánchez-Arellano, J. Madrigal-Melchor, and I. Rodríguez-Vargas, Scientific reports **9**, 1 (2019).
- [42] F. Tian, D. Duan, D. Li, C. Chen, X. Sha, Z. Zhao, B. Liu, and T. Cui, Scientific reports **4**, 1 (2014).
- [43] A. Sharma, A. A. Tulapurkar, and B. Muralidharan, Journal of Applied Physics **129**, 233901 (2021).
- [44] A. Sharma, A. A. Tulapurkar, and B. Muralidharan, Applied Physics Letters **112**, 192404 (2018).
- [45] S. Datta, *Lessons from Nanoelectronics: A New Perspective on Transport—Part B: Quantum Transport* (World Scientific, 2018).
- [46] D. C. Ralph and M. D. Stiles, Journal of Magnetism and Magnetic Materials **320**, 1190 (2008).
- [47] S. Datta, *Quantum transport: atom to transistor* (Cambridge university press, 2005).
- [48] S. Datta, *Electronic transport in mesoscopic systems* (Cambridge university press, 1997).
- [49] D. Ralph, Y.-T. Cui, L. Liu, T. Moriyama, C. Wang, and R. Buhrman, Philosophical Transactions of the Royal Society A: Mathematical, Physical and Engineering Sciences **369**, 3617 (2011).
- [50] B. Tudu and A. Tiwari, Vacuum **146**, 329 (2017).
- [51] R. Prakash, B. P. S. Rathore, and D. Kaur, Journal of Alloys and Compounds **726**, 693 (2017).
- [52] S. Ikeda, K. Miura, H. Yamamoto, K. Mizunuma, H. Gan, M. Endo, S. Kanai, J. Hayakawa, F. Matsukura, and H. Ohno, Nature materials **9**, 721 (2010).
- [53] D. Datta, B. Behin-Aein, S. Datta, and S. Salahuddin, IEEE Transactions on Nanotechnology **11**, 261 (2011).
- [54] B. Datta, IEEE Transactions on Nanotechnology **11**, 261 (2012).
- [55] S.-H. Yang, K.-S. Ryu, and S. Parkin, Nature nanotechnology **10**, 221 (2015).
- [56] A. M. Deac, A. Fukushima, H. Kubota, H. Maehara, Y. Suzuki, S. Yuasa, Y. Nagamine, K. Tsunekawa, D. D. Djayaprawira, and N. Watanabe, Nature Physics **4**, 803 (2008).
- [57] H. Sato, E. Enobio, M. Yamanouchi, S. Ikeda, S. Fukami, S. Kanai, F. Matsukura, and H. Ohno, Applied Physics Letters **105**, 062403 (2014).
- [58] M. Gajek, J. Nowak, J. Sun, P. Trouilloud, E. O'sullivan, D. Abraham, M. Gaidis, G. Hu, S. Brown, Y. Zhu, *et al.*, Applied Physics Letters **100**, 132408 (2012).
- [59] A. Manchon, J. Železný, I. M. Miron, T. Jungwirth, J. Sinova, A. Thiaville, K. Garello, and P. Gambardella, Reviews of Modern Physics **91**, 035004 (2019).
- [60] S. Ikeda, J. Hayakawa, Y. Ashizawa, Y. Lee, K. Miura, H. Hasegawa, M. Tsunoda, F. Matsukura, and H. Ohno, Applied Physics Letters **93**, 082508 (2008).